Palaeogeography, Palaeoclimatology, Palaeoecology 581 (2021) 110639

Contents lists available at ScienceDirect

Palaeogeography, Palaeoclimatology, Palaeoecology

journal homepage: www.elsevier.com/locate/palaeo

Integrated stratigraphy of the middle-upper Eocene Souar Formation (Tunisian dorsal): Implications for the Middle Eocene Climatic Optimum (MECO) in the SW Neo-Tethys

Jihede Haj Messaoud [a,b,g,*], Nicolas Thibault [a], Brahimsamba Bomou [c], Thierry Adatte [c], Johannes Monkenbusch [a], Jorge E. Spangenberg [d], Mohammed H. Aljahdali [e], Chokri Yaich [f,g]

[a] Department of Geosciences and Natural Resource Management, University of Copenhagen, Øster Voldgade 10, DK-1350 Copenhagen C., Denmark
[b] The Ali I. Al-Naimi Petroleum Engineering Research Center, King Abdullah University of Science and Technology, Thuwal, Saudi Arabia
[c] Institute of Earth Sciences (ISTE), University of Lausanne, Geopolis, CH-1015 Lausanne, Switzerland
[d] Institute of Earth Surface Dynamics (IDYST), University of Lausanne, Geopolis, CH-1015 Lausanne, Switzerland
[e] Marine Geology Department, Faculty of Marine Sciences, King Abdulaziz University, Jeddah 21589, Saudi Arabia
[f] Laboratory of Sediment Dynamics and Environment, Sfax National School of Engineers, PB 1173, 3038, Univ. of Sfax, Tunisia
[g] Sfax National Engineering School, PB 1178, Soukra Road km 4, Sfax 3038, University of Sfax, Road of the Airport km 0.5, Tunisia

ARTICLE INFO

Editor: A Dickson

Keywords:
Bayesian modelling
X-ray diffraction
Global warming
Calcareous nannofossils
Carbon isotope stratigraphy
X-ray fluorescence

ABSTRACT

Calcareous nannofossil biostratigraphy and carbon-isotope stratigraphy on bulk organics of the middle-upper Eocene Souar Formation (Tunisia) allow for a refined stratigraphy of this interval in the southwestern Neo-Tethys margin. The Souar Formation represents the deepest sedimentary deposits of the central northern Tunisian Basin and was only dated previously by coarse data on planktonic foraminifera. Together with our new data, a correlation is proposed to previous Tunisian records of the Halk El Menzal carbonate platform to the NE and shallow-water deposits of central Tunisia to the SW, which leads us to the erection of a synthetic stratigraphic chart of the middle-upper Eocene in central and northeastern Tunisia. Our results allow for a review of the accurate position of the Lutetian / Bartonian and the Bartonian / Priabonian stage boundaries in Tunisia relative to calcareous nannofossil biohorizons. We apply Bayesian statistics to build our age-depth model which points to a hiatus in the Lutetian (CNE12 Zone) that we relate to the middle Lutetian regressive sequence leading to the Lu-4 M-cycle. Radiolarian-rich sediments and cherts of the late Lutetian and early Bartonian are interpreted as a response to an increase in productivity, tied to the seasonal upwelling of nutrient-rich waters. Correlation to other sections in Tunisia highlights the strong contrast in facies between the carbonate-rich sequences of the edges of the dorsal and the silica-rich deposition in the Souar Formation. This contrast is particularly pronounced in the interval before and across the Middle Eocene Climatic Optimum (MECO) characterized by a maximum of nummulitic carbonate production on the platform and a minimum of carbonate production in the deep basinal parts of the Tunisian dorsal, rather dominated by silica-rich sediments.

1. Introduction

Following the high temperatures of the Early Eocene Climatic Optimum (EECO, ~52–50 Myr), the ~17 Ma cooling trend that culminated in the Eocene-Oligocene Transition (EOT, 33.88 Ma, Westerhold et al., 2014; Galeotti et al., 2016; Messaoud et al., 2020).was interrupted by short-lived hyperthermal events (Miller et al., 1987; Zachos et al., 1996, 2008; Zachos, 2001; Coxall et al., 2005; Edgar et al., 2007). One major Middle Eocene hyperthermal is the Middle Eocene Climatic Optimum (MECO, Bohaty and Zachos, 2003; Bohaty et al., 2009). It was identified as a transient negative oxygen isotopic excursion of about −1.0‰ (in benthic foraminifera, Bohaty and Zachos, 2003) with noticeable peak warming conditions at the C18r/C18n.2n magnetochron boundary (Bohaty et al., 2009). A ~ 4–6 °C warming of the surface and deep

* Corresponding author at: Department of Geosciences and Natural Resource Management, University of Copenhagen, Øster Voldgade 10, DK-1350 Copenhagen C., Denmark.
E-mail addresses: jhm@ign.ku.dk (J.H. Messaoud), nt@ign.ku.dk (N. Thibault), brahimsamba.bomou@unil.ch (B. Bomou), thierry.adatte@unil.ch (T. Adatte), jomo@ign.ku.dk (J. Monkenbusch), Jorge.Spangenberg@unil.ch (J.E. Spangenberg), maljahdli@kau.edu.sa (M.H. Aljahdali).

https://doi.org/10.1016/j.palaeo.2021.110639
Received 12 April 2021; Received in revised form 19 August 2021; Accepted 25 August 2021
Available online 3 September 2021

waters was estimated for this event in the early Bartonian (e.g., Bohaty et al., 2009; Edgar et al., 2010, 2020; Sluijs et al., 2013) while a milder Late Eocene warming event characterizes the Priabonian (Fig. 1, Bohaty and Zachos, 2003). In parallel, major continental plate reorganization led to the opening and closure of ocean basins and the uplift of mountain belts (Kennett, 1977). The opening of the Tasmanian-Antarctic Gateway and the opening of the Drake Passage yielded to the onset of a circum-Antarctic pathway eventually leading later to the Antarctic glaciation at the Eocene-Oligocene transition (e.g., Barker and Burrell, 1977; Bohaty and Zachos, 2003; Exon et al., 2004; Wei, 2004; Livermore et al., 2005; Sijp et al., 2014).

At lower latitudes, the continuing convergence of the African-Arabian craton and India toward Eurasia induced a multi-phase uplift of the Alpine-Himalayan orogenic system, which represents a threshold that caused the Late Eocene palaeoceanographic restriction of the Neo-Tethys (e.g., Garzanti et al., 1996; Jovane et al., 2007b; Sijp et al., 2014; Vahlenkamp et al., 2018). Although the origin of the MECO is still controversial in current paleoclimatic models (e.g., Giorgioni et al., 2019; Jovane et al., 2009), it is considered the most significant Middle Eocene hyperthermal in terms of duration and magnitude (Bohaty and Zachos, 2003; Bohaty et al., 2009). This ~500-kyr long event, coined as the MECO is now identified in deep-sea cores from the Indian, Atlantic, Pacific, and Southern Oceans as well as land-based marine sections in China, Turkey, Italy, United Kingdom, and North America (e.g., Bohaty and Zachos, 2003; Jovane et al., 2007a, 2007b; Villa et al., 2008; Luciani et al., 2010; Spofforth et al., 2010; Dawber and Tripati, 2011; Toffanin et al., 2011; Boscolo Galazzo et al., 2013; Methner et al., 2016; Giorgioni et al., 2019; Shi et al., 2019). At low-latitudes sites, the MECO witnessed several faunal and floral events that are used as excellent biostratigraphic markers such as the acme of planktonic foraminifera *Orbulinoides beckmanni* (Edgar et al., 2010; Agnini et al., 2011; Luciani et al., 2020), and the base of the coccolithophorid *Reticulofenestra stavensis* (syn. *Dictyococcites bisectus*, Edgar et al., 2010, 2020). Sediments of that age interval are well-exposed in Tunisia and thus constitute excellent archives for the expression of middle to Late Eocene global climatic changes in the southern Neo-Tethys. The main aim of this study is, therefore (1) to establish an integrated stratigraphic framework for the southern Neo-Tethys deposits across the middle to Late Eocene and (2) to better understand the potential relationship of major facies changes in the Tunisian dorsal observed across the Lutetian-Priabonian interval to the MECO event and the restriction of the Neo-Tethys.

2. Material and methods

2.1. Geologic settings

The study area (36°13′27.07″N; 10°1′23.77″E) is located in the East of Jebel Zaghouan (northeastern Tunisia), 8 km ESE of the Souar Formation locality type defined by Burollet (1956). The Zaghouan mountain (Fig. 2a) is an Atlasic structure trending NE-SW and belongs to the ranges of the Tunisian dorsal (e.g., Ben Ferjani et al., 1990; Mejri et al., 2006), between the Pelagian platform to the east and the thrust belt of the Atlas mountains to the west (e.g., Burollet, 1956; Burollet and Ellouz, 1986; Ben Ayed, 1993; Melki et al., 2011). The investigated Souar section is situated in a graben structure (NE jebel Fkerine), delineated by NW-, E- and sometimes N- striking normal faults formed during the Jurassic (e.g., Soussi et al., 1999; Soussi and Ben Ismaïl, 2000; Bouaziz et al., 2002; Enay et al., 2005). During the Paleogene, the graben structure was remobilized when the regional structural context changed into a NE-SW extension (e.g., Chihi, 1995; Bedir et al., 1996; Bouaziz et al., 2002). The continuous subsidence in the Pelagian platform during the middle Eocene is responsible for the deposition of a thick globigerinid-rich clay sequence. The thickness of the Souar Formation is up to 1100 m in the locality type (Burollet, 1956). For this study, and due to exposure conditions, only 604 m of this section in its central part could be studied and sampled. The studied section is

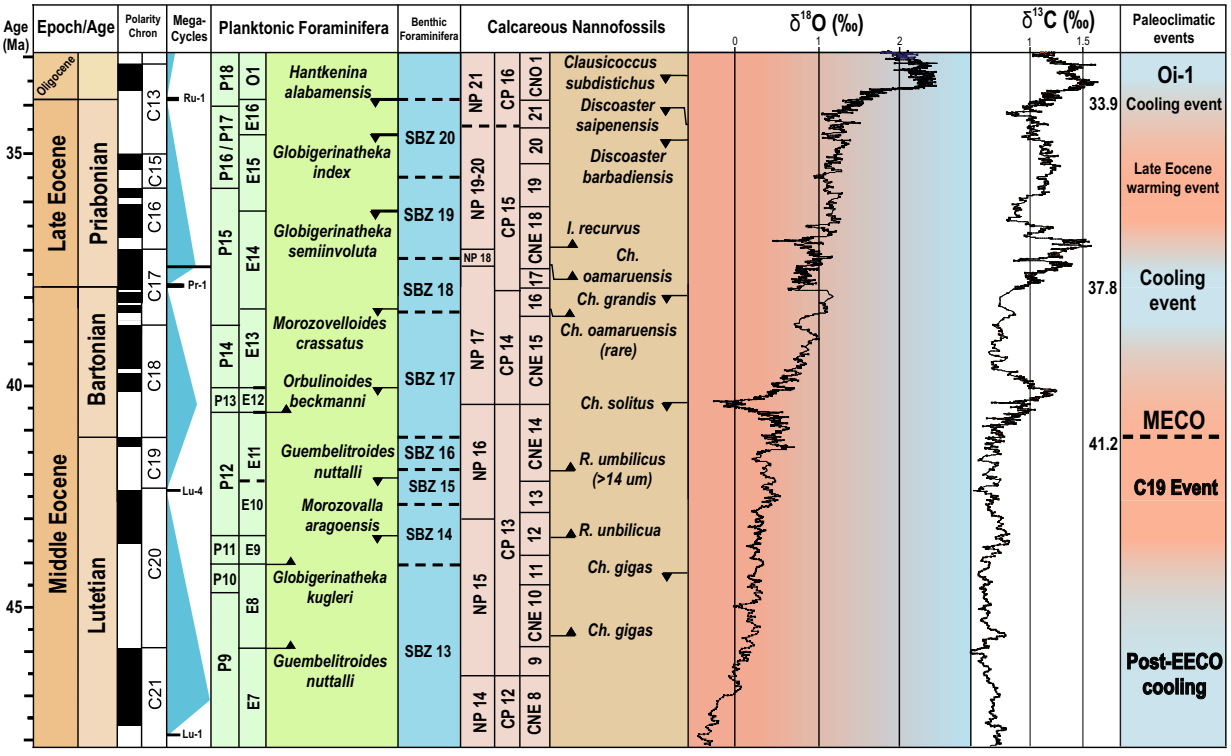

Fig. 1. Middle-Late Eocene stratigraphic subdivisions, geomagnetic polarity scale, zonation of planktonic foraminifera (Wade et al., 2011), larger benthic foraminifera (Serra-Kiel et al., 1998), and calcareous nannofossil (Agnini et al., 2014; Martini, 1971; Okada and Bukry, 1980). Stable isotope stratigraphy is modified from tables in the Pacific Equatorial Age Transect program (Palike et al., 2010). The main Paleogene transgressive-regressive trends are modified from Hardenbol et al. (1998). $\delta^{13}C$ and $\delta^{18}O$ are from Zachos et al. (2001).

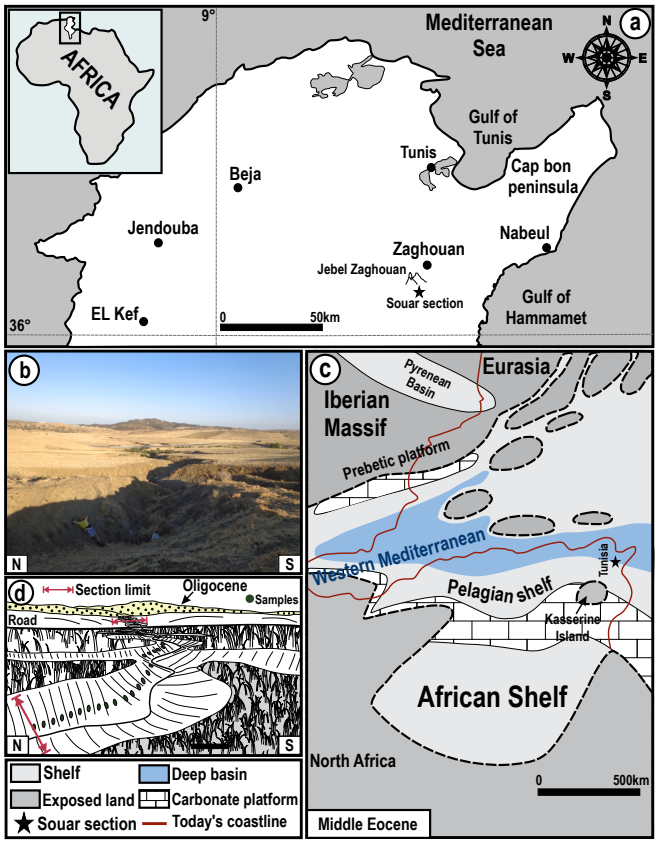

Fig. 2. (a) Geographic map of north Tunisia with the location of the studied Souar section. (b) Outcrop photograph of sediments at the Souar section viewed from the West. (c) Middle Eocene paleogeography of the Western Mediterranean realm (modified after Höntzsch, 2011). (d) Schematic interpretation of (b) showing the limits of the studied section and the adopted sampling strategy.

interrupted by one sampling gap at 504–506 m (2 m) covered by thick recent scree deposits and vegetation.

2.2. Calcareous nannofossil (CN) analysis

Ninety-four samples (~6.4 m resolution) have been analysed for calcareous nannofossil content (Appendix 1). The slides were prepared following the drop technique as described in Thibault and Gardin (2006). Slides were observed with a Leica DM750P polarized microscope with a magnification of 1000× and an additional 1.25 lens (magnification 1250×). Major fluctuations in the total nannofossil abundance were observed through the section, hence, we report the total number of specimens per field of view (N/FOV). The total number of specimens per field of view is also reported as N/mm^2 with the area of one FOV of 0.045 mm^2. Due to a drastic decrease in the total absolute abundance of calcareous nannofossils across the Lutetian/Bartonian transition, we also evaluated the relative abundance of calcareous nannofossil species over a total of 300 specimens. Important abundance patterns of relevant biostratigraphic markers have generally been documented in deep-sea sites and Italian outcrop sections by using the number of specimens in N/mm^2 (e.g., Monechi et al., 2000; Agnini et al., 2006). However, as shown further, this is not possible here due to the drastic decrease in the total nannofossil abundance across the Lutetian/Bartonian transition, and therefore, these patterns are documented here using relative abundances. We applied the four distinct zonation schemes (NP, CP, MNP, and CNE) of respectively Martini (1971), Okada and Bukry (1980), Fornaciari et al. (2010), and Agnini et al. (2014). To comply with the latter CNE scheme, we used Base (B) and Top (T), to describe the stratigraphic lowest and highest occurrences of taxa, respectively, as described in Agnini et al. (2014). The latter scheme of Agnini et al. (2014) also uses the concepts of Bc (for Base common or consistent) and Tc (for Top common or consistent) biohorizons. The Bc biohorizon corresponds to where the abundance of a marker species becomes consistent and/or more abundant whereas the Tc biohorizon is positioned where the abundance of an index species starts to be discontinuous usually with lower abundances (Agnini et al., 2014). Taxonomically, we did not make any distinction between genera *Cribrocentrum*, *Dictyococcites,* and *Reticulofenestra* as in Perch-Nielsen (1985) and rather followed Young (1990) who merges them into one single genus of *Reticulofenestra*. There is considerable confusion in the literature in the taxonomy of Reticulofenestrids. The genus *Dictyococcites* is distinguished from *Reticulofenestra* by a central area that is covered by two layers or more of elements while *Reticulofenestra* has a very fine, simple central net (Perch-Nielsen, 1985). Some authors define *D. scrippsae* for specimens <10 μm and *D. bisectus* for specimens >10 μm, while *D. hesslandii* (not considered in our study) comprises specimens of 3 to 7 μm with a central area nearly closed by inner tube cycle. Fornaciari et al. (2010) and Agnini et al. (2014) kept the distinction between the two genera and consider *D. scrippsae* as a junior synonym of *D. hesslandii*, thus comprising specimens <10 μm in *D. scrippsae* and specimens >10 μm belong to *D. bisectus*. However, the holotype of *R. bisecta* (*Syracosphaera bisecta* Hay et al., 1967) is 8.2 μm in length, so theoretically, we should not use a definition of *R. bisecta* (or *D. bisectus*) as being >10 μm when the holotype falls outside of this definition. The holotype of *R. scrippsae* (6–12 μm based on the original definition of *Dictyococcites scrippsae* by Bukry (1971)) is indistinguishable from *R. bisecta*, and is a junior synonym by year of publication.

Bown (2005) and Dunkley Jones et al. (2008) have adopted an approach where *Dictyococcites* is obsolete and rather consider *D. scrippsae* and *D. bisectus* forms as various species of *Reticulofenestra* within the *R. bisecta* group sensu lato, with *R. bisecta* sensu stricto comprising medium to large specimens (~5 to 10 μm) while *R. stavensis* (syn. *D. bisectus* of Agnini et al., 2014) comprises large to very large forms >10 μm, and we follow their taxonomy here. Although this taxonomic approach is likely more consistent with the definition of species holotypes, it generates additional confusion to the biostratigraphic scheme of Agnini et al. (2014) who uses the base of *D. bisectus* (>10 μm, syn. *R. stavensis* in our study) to define the CNE14/CNE15 zonal boundary. Our concept of *R. hillae* comprises specimens >9 μm, and our concept of *R. umbilicus* comprises specimens >14 μm, following the taxonomic concept of Backman and Hermelin (1986). We also made a distinction between *C. pelagicus* (<13 μm) and *C. eopelagicus* (>14 μm). Finally, we did not make any distinction between morphotypes (A) and (B) of *Sphenolithus furcatolithoides* (Shamrock, 2010).

2.3. Abundance of radiolarians

The abundance of radiolarians in the section has been calculated on a total of 32 samples spanning the first 500 m of the Souar section (Appendix 6). Collected samples were washed after treatment with H_2O_2 and sieved into four-grain size fractions (>500 μm, >250 μm, >100 μm, and > 63 μm). Different kinds of microfossils (ostracods, planktic and benthic foraminifera, radiolarians, debris of bivalves, and unidentified bioclasts) have been picked and counted from the different size fractions with an Optika stereomicroscope. Sieving and counting were performed by an amateur geology student from Sfax who unfortunately did not weigh the different size fractions after sieving 300 g of material, but instead examined the abundance of various microfossils from a subset of 10 g of each sieved size fraction. Radiolarians were found and counted for their absolute abundance from the >63 and > 100 μm size fractions while carbonate microfossils, e.g., ostracods, benthic and planktonic foraminifera were found and counted in the >250, >100, and > 63 μm size fractions (Appendix 2). As we cannot report with accuracy the total number of each kind of microfossils per gram of sediment, we show instead the ratio between the total number of counted radiolarians to the

total number of calcitic microfossils (ostracods + foraminifera) to highlight the progressive replacement of the carbonated microfauna by siliceous microfauna within the radiolarian-rich clays of the Djebel Zaghouan Mb. (Fig. 3).

2.4. Bulk mineralogy

A total of 90 bulk-rock samples (Appendix 4) were analysed at the Institute of Earth Sciences of the University of Lausanne (ISTE-UNIL) using an X-TRA Thermo-ARL Diffractometer following the Kübler's procedure (Kübler, 1987; Adatte et al., 1996). The method for semi-quantitative analysis of the bulk-rock mineralogy used external standards with an error varying between 5 and 10% for the phyllosilicates and 5% for grain minerals. The files generated are raw data (.RD), which are transformed in routine by the software (WinXRD 2.0–6 Thermo-Fischer program) into calculated (.NI) files. The calculations include Fast Fourier noise filter, background subtraction, and Ka2 stripping. The measurements are generally made on calculated files. A Detrital Index (DI) was calculated using the sum of phyllosilicates, quartz, K-feldspar, and plagioclase divided by calcite contents.

2.5. Major elements (HH-XRF)

The content in selected elements (Ca, Al, Ti, Si) is reported here from the measurement of a total of 186 samples by an Innov-X Olympus Delta Premium 600 handheld energy-dispersive X-ray fluorescence spectrometer (HH-XRF) mounted in a certified portable workstation (Appendix 5). Plugs were covered with cling film, similar to the calibration process (Ahm et al., 2017). Plugs have been analysed twice for 2 min using both the 10 kV and 40 kV beam settings with an Rh tube and a large-area, high-performance silicon drift detector (cf. Ahm et al., 2017). Data were acquired using the Geochem Mode that uses a Fundamental Parameters correction method integrated into the Innov-X Delta PC software, where 131 certified standards have been used for calibration. Instrument calibration was checked after every 10 measurements with a standardized metal alloy coin supplied by the manufacturer. To provide a better resolution of trends in calcite content through the section, we recalculated the % $CaCO_3$ using the correlation of common samples measured both for % Ca (HH-XRF) and % Calcite (XRD), by assuming that the source of Ca predominantly originates from calcite. Out of the 90 samples measured, 6 outliers correspond to either the highest values in % calcite or % Ca and may be related to the presence of dolomite and/or other carbonate minerals. These outliers were not taken into account to test for the correlation. An equation with a zero intercept was calculated and applied to % Ca (supplementary materials).

2.6. Bulk organics carbon isotopes

A total of 77 samples (Appendix 2) were analysed for carbon isotopes in bulk organic matter (δ 13Corg) at the Institute of Earth Surface Dynamics of the University of Lausanne (IDYST-UNIL) by flash combustion on a Carlo Erba 1108 elemental analyser (EA) connected to a Thermo Fisher Scientific Delta V Plus (Bremen, Germany) isotope ratio mass spectrometer (IRMS) that was operated in the continuous helium flow mode via a Conflo III split interface (EA/IRMS). The isotope ratios were expressed as the per mil (‰) deviation relative to the Vienna Pee Dee Belemnite scale (V-PDB). The calibration and normalization of the measured isotopic ratios to the VPDB scale were performed with a 4-point calibration, using international reference materials and UNIL in-house standards (Spangenberg et al., 2006). The standards used for

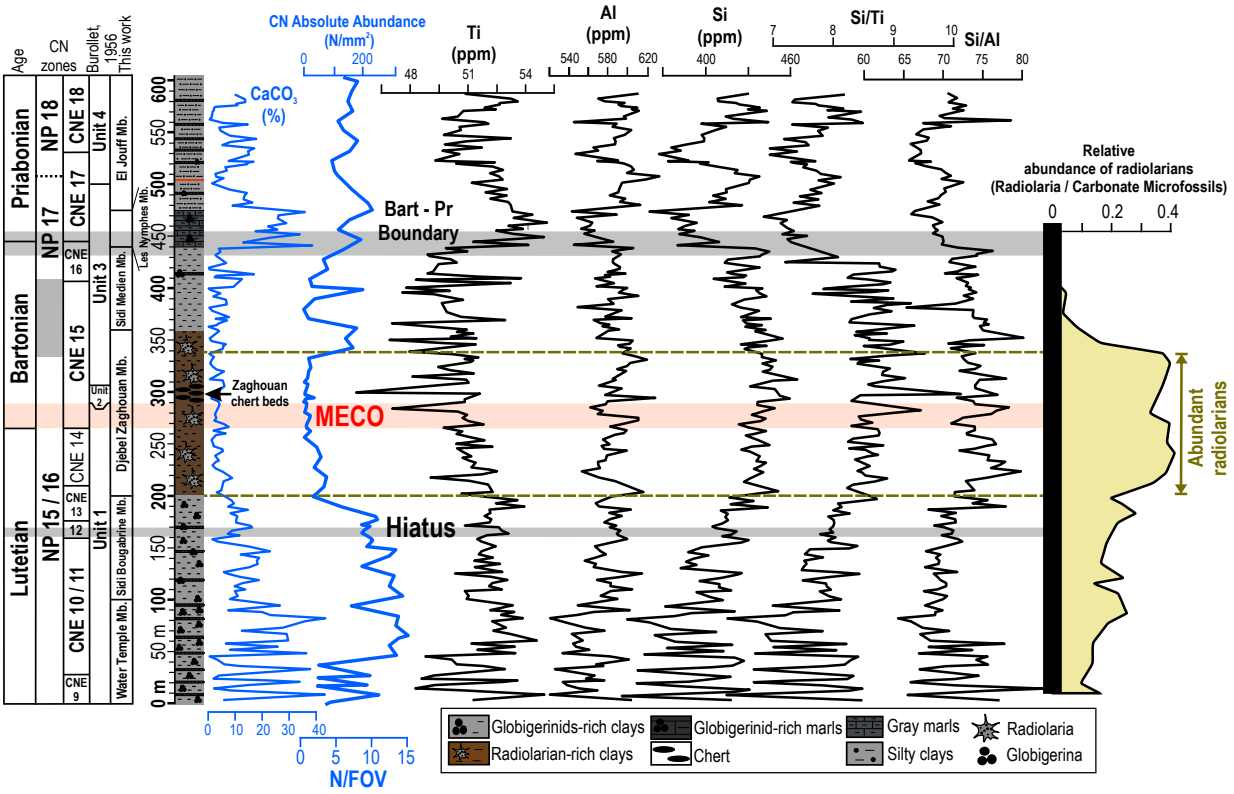

Fig. 3. Calcareous nannofossils biostratigraphy, lithostratigraphy, and depth profiles for the recalculated CaCO3 (%), CN specimens per mm^2, Ti, Al, Si, Si/Ti, Si/Al, and the abundance of radiolarian / (forams + ostracods)). The horizontal pink area marks the biostratigraphic interval of the MECO and the two gray areas mark the Lutetian hiatus and the Bartonian-Priabonian boundary. Note the interval between 200 m and 360 m shows low carbonate content and low Ti whereas Al is stable along the Souar section. Combining these results with the observed abundant radiolarian compared to foraminifera and ostracods with an increase in Si during the same interval suggests that a part of the high Si content between 200 m and 360 m is related to biogenic silica. (For interpretation of the references to colour in this figure legend, the reader is referred to the web version of this article.)

$\delta^{13}C_{org}$ were UNIL-Glycine ($\delta^{13}C_{VPDB} = -26.10 \pm 0.05‰$), UNIL-Urea-1 ($\delta^{13}C_{VPDB} = -43.89 \pm 0.03‰$), UNIL-Pyridine ($\delta^{13}C_{VPDB} = -29.24 \pm 0.06‰$), and USGS-24 graphite ($\delta^{13}C = -16.05 \pm 0.04‰$). The reproducibility of the EA/IRMS analysis was determined by replicate analyses of laboratory standards and international reference materials and was better than 0.1‰ (1 SD).

2.7. Bayesian age-depth modelling

The Bacon modelling is a new approach for a chronology that uses Bayesian statistics to reconstruct Bayesian accumulation histories for sedimentary deposits. The section is divided into many thin vertical intervals and through millions of Markov Chain Monte Carlo (MCMC) iterations, best estimates of sedimentation rates are calculated for each of these sections intervals based on piece-wise linear interpolation (Brooks et al., 2011). Combined with an estimated starting date for the first interval, these accumulation rates then form the age-depth model. Hiatuses can be introduced and constrained by prior information (*hiatus.* max). An age model was developed using the Bchron R software package (https://CRAN.R-project.org/package=rbacon). We ran the Bacon model for every 1 m depth intervals (as in Blaauw and Christeny, 2011; De Vleeschouwer and Parnell, 2014; Sprain et al., 2019; Eldrett et al., 2020). The input for the Bacon script includes: Min Age = 36,000 ka, Max Age = 47,000 ka, Acc. Mean = 20, and 11 intervals of 65 m (see Appendix 7 for details). Two distinct age models are considered, one with a hiatus within the CNE12 Zone (Fig. 9) and one without any hiatus (supplementary materials).

3. Results

3.1. Lithostratigraphy

The original lithological description adopted by Burollet (1956) was as follows (Fig. 3):

- ➢ Unit 1 is a 290-m interval of silty gray clays, some levels are marly, especially in the lower part. The identified planktonic foraminifera assemblages were named by Dalbiez (1955) the *Clavulinoides* I Zone (see paragraph 4.1).
- ➢ Unit 2 is a 15-m interval of chert beds that was previously described as fine glauconitic sandstone by Dalbiez (1955) and Burollet (1956)
- ➢ Unit 3 is a 195 m thick package of gray to brown clays. The microfauna is abundant and characterizes the "*Bulimina* 101 Zone " (Burollet, 1956).
- ➢ Unit 4 is a 104 m package of gray clays and marls unit, with gypsum crystals. The lower part of this unit contains a microfauna of the *Bulimina* 101 Zone (Burollet, 1956).

Burollet (1956) essentially defined these units from a mix of poorly accurate field observations in lithology and content in foraminiferal assemblages. Our field observations and results obtained from variations in carbonate content and major elements from XRF suggest a lithostratigraphic subdivision of the Souar Formation that is quite different from that adopted by Burollet (1956). In particular, our observations of a prominent radiolarian-rich interval from 200 to 370 m call for the definition of new Members (Mb.) within the Souar Formation.

The Water Temple Mb. (0 to 100 m) is a globigerinid-rich unit of middle Lutetian age characterized by alternating clays and marls, with marls reaching %$CaCO_3$ values of 30 to 40%, and clays are generally below 10%, sometimes being completely carbonate-free. The name derives from ancient Roman ruins in the Zaghouan National Park from which water was sourced and flown along Roman aqueducts to Carthage.

The Sidi Bougabrine Mb. (100 to 200 m) is a gray clay unit of late Lutetian age characterized by a stepwise decrease in calcium carbonate from ca. 20% at the base to <5% at the top. We note two marly intervals with local maxima in % $CaCO_3$ that interrupt this long-term decreasing trend centered around 147 and 179 m while near pure clayey intervals occur at 126 and 158 m. The name derives from the Sidi Bougabrine Mausoleum inside the Zaghouan National Park.

The Djebel Zaghouan Mb. (200 to 360 m) is defined as a gray radiolarian-rich clay unit, of late Lutetian to Bartonian age, with % $CaCO_3$ values <10%, fluctuating around a mean of 5%. These clays are muddy, unconsolidated, and contain few foraminifera and ostracods, therefore this deposit cannot be considered as a radiolarite. This unit is also characterized by the lowest number of nannofossil specimens per mm^2 (less than 20) but sediments are not completely barren of nannofossils, thus attesting that this sedimentary unit is widely dominated by a biosiliceous production with an adventitious carbonate fauna and flora. Within this unit, five distinct 10 to 15 cm thick beds of glauconitic chert stand out from 290 to 307 m in the early Bartonian. This sub-unit corresponds to Unit 2 of Burollet (1956) although he distinguished only two beds and described them as sandstone. We distinguish this informal subunit here as "Zaghouan chert beds" as they may prove useful for stratigraphic correlation. These chert beds probably mark a peak of biosiliceous production. The name of the Mb. derives from the Djebel Zaghouan mountain.

The Sidi Medien Mb. (360 to 440 m) is defined as a gray clay unit that is essentially distinguished from the Djebel Zaghouan Mb. below by its distinctively lower abundance of radiolarians (Fig. 3). The name of this Mb. derives from the Sidi Medien Mosque in the area of the Zaghouan National Park.

The Les Nymphes Mb. (440 to 475 m) is an early Priabonian carbonate-rich unit that stands out from intervals below and above. The unit is gray argillaceous marl, characterized by average % $CaCO_3$ values of 26%, abundant foraminifera, and higher total abundance in calcareous nannofossils. A drastic decrease in Si content is also logically recorded within this unit (Fig. 3). The name derives from the eponym Hotel in Zaghouan.

The El Jouff Mb. (475 to 600 m) is a Priabonian unit of alternating, gray silty clays and globigerinid-rich marls with the presence of scarce macroscopic gypsum. Calcareous nannofossils and foraminifera are common. Although the description of this unit is not very different from that of the Lutetian Water Temple Mb., it must be noted that the argillaceous marls of this unit are also silty and have a lower carbonate content as compared to those of the Water Temple Mb. The El Jouff Mb. is also siltier than the Water Temple Mb. The name derives from the El Jouff village situated South of the Zaghouan National Park.

3.2. Calcareous nannofossil

Preservation and absolute abundance of the nannofossil assemblage vary along the section. The preservation is moderate from the base of the section up to 190 m, moderate to good from 200 to 305 m, good from 315 to 475 m, and moderate from 480 m to the top of the section. The dissolution seems to affect moderately the assemblage with a significant dissolution interval within the CNE12 Zone. The total nannofossil abundance ranges between 2 and 325 (N/mm^2) throughout the entire section (Fig. 3). Between the base of the section up to 38 m, the nannofossil abundance fluctuates between 44 and 207 (N/mm^2), while the abundance remains stable around an average of 260 N/mm^2 from 47 to 225 m (Fig. 3). A distinct drop in the nannofossil abundance that drastically declines to 4 N/mm^2 occurs at 257 m and the abundance remains around this low value up to 333 m (Fig. 3). Higher abundance values up to 166 N/mm^2 are observed between 340 and 371 m and a return to very low abundance occurs at 380 m. A long-term increase in absolute abundance is observed from 380 to 476 m, interrupted by a punctual maximum up to 185 N/mm^2 at 399 m. Maximum values of 214 N/mm^2 are reached at 476 m. The remaining section shows abundance values fluctuating around 140 N/mm^2.

The assemblage is largely dominated by placoliths belonging to the genus *Reticulofenestra*. Dominant and common species are

Reticulofenestra dictyoda, Pontosphaera multipora, *C. pelagicus*, *Discoaster barbadiensis*, *Discoaster saipanensis, Discoaster deflandrei, Sphenolithus moriformis*, and *Braarudosphaera bigelowii* (Figs. 4 and 5). In the present study, the very low total nannofossil abundance observed in most samples from 200 to 430 m as compared to deep-sea sites and sections on which the CNE scheme is based, prevented the use of trends in absolute nannofossil abundance to compare to patterns delineated in Agnini et al. (2014), and somewhat probably prevented any clear observation of Bc or Tc biohorizons.

All our recorded biohorizons are either Bases or Tops. However, our observations are supported by patterns detected in the relative abundance of these species showing that B and T biohorizons systematically correspond to well-defined events with a clear increase and/or decrease in abundance, respectively, as well as with no record of discontinuous occurrences below or above (Fig. 5). Hence, it is likely that B and T biohorizons of relevant taxa used here actually coincide with Bc and Tc biohorizons of the Agnini et al. (2014) scheme.

The B *C. gigas* at 28 m (Fig. 5) defines the CNE9/CNE10 zonal boundary of Agnini et al. (2014) and the CP13a/CP13b zonal boundary of Okada and Bukry (1980). Accordingly, the first 28 m is assigned to the upper part of the *Nannotetrina alata* group Base Zone CNE9 (Fig. 5). At 76 m, B. *S. furcatolithoides* confirms that this interval belongs to CNE10. The absence of *S. cuniculus* in the analysed assemblages did not allow the separation between CNE10/CNE11. These two zones correspond to the middle-upper part of Zone NP15. At 160 m, the top of *C. gigas* is recorded and marks the base of CNE12. The base of NP16 originally defined by Martini, (1971) by the last occurrence of *Blackites gladius* is of little use here as this species was not observed at all in our dataset but this level is considered to correlate approximately with the top of *C. gigas* (Perch-Nielsen, 1985).

The B of *R. umbilicus* is noted at 175 m (Fig. 5) and corresponds to a level after which this species is consistently present with a rather similar contribution in the assemblage throughout the section, therefore we consider that this base occurrence in our section correlates with the Bc of *R. umbilicus* that defines the base of CNE13(e.g., Agnini et al., 2014; Fioroni et al., 2015). Consequently, the 160–175 m interval corresponds to the *Nannotetrina* spp. Partial Range Zone (CNE12). The B of *R. reticulata* at 209.5 m also marks a level after which the species is consistently present in the assemblage and therefore, we consider here that this level correlates with the Bc of the species that defines the base of CNE14. As in the Agnini et al. (2014) scheme, we note the top of *S. furcatolithoides* within the topmost part of CNE14 at 257 m. The base of *R. stavensis* (syn. *D. bisectus* of Agnini et al. (2014)) at 266 m defines the base of zone CNE15. Similar to Agnini et al. (2014) zonal scheme, we observe the base of *S. obtusus* at 333 m, followed by the top of *S. spiniger* at 352 m which likely correlates to its recorded Tc in the Agnini et al. (2014) zonal scheme within the lower half of CNE15, while the top of *S. obtusus* at 409 m marks the base of CNE16. The absence of *Chiasmolithus solitus* in our studied samples hindered us to distinguish the base of NP17. As noted by Agnini et al. (2014), this species is sporadic at the top of its range, making the base of this zone difficult to distinguish and reinforcing the usefulness of the alternative Agnini et al. (2014) scheme. However, Bown and Dunkley Jones (2012) indicate that the range of *S. obtusus* spans upper NP16 to NP17, the top of this taxon is situated within the upper half of NP17. Therefore, the range of *S. obtusus* in our study somewhat delineates a zone of uncertainty for the NP16/NP17 boundary (gray zone in Fig. 5).

A coinciding B and Bc of *R. erbae* is recorded at 447 m (Fig. 5), similarly to what we have described above for *R. umbilicus* and *R. reticulata*, and we consider that this level likely correlates with the Bc of the species that defines the base of CNE17 in the Agnini et al. (2014) zonal scheme. Although *Chiasmolithus oamaruensis* was very scarce, the top of *Chiasmolithus grandis* at 509 m is alternatively used to approximate the base of NP18 and confirms a Priabonian age (Marino and Flores, 2002; Agnini et al., 2014). The top of *R. erbae* at 532 m is sharp with no rare or discontinuous occurrence patterns further up the section (Fig. 5), therefore, the bioevent is used here to define the top of CNE17. We note that the top of *C. grandis* at 509 m thus falls within the upper third of CNE17 versus the lower half of this zone in the scheme which accounts for a slight discrepancy with this standard zonation.

3.3. Relative abundance in radiolarians

The ratio of radiolarians to total carbonate microfossils (ostracods + foraminifera) steadily increases from the base of the section (ca. 0.1) to around 200 m where it reaches up to 0.25. A sudden increase in this ratio is observed at 200 m that defines the base of the Djebel Zaghouan Mb. Throughout most of this member, this ratio remains around values of 0.4. The uppermost part of the Djebel Zaghouan Mb. records a sharp decrease in this ratio and the top is defined when the ratio returns to values below 0.2 at 360 m (Fig. 3). The lowermost part of the Sidi Medien Mb. shows a progressive decrease in the ratio leading up to the complete absence of radiolarians above 410 m.

3.4. Bulk-rock mineralogy

In the Souar section, phyllosilicates, quartz, calcite, and gypsum represent the dominant phases (Fig. 6). K-feldspar, plagioclase, dolomite, goethite, ankerite, and pyrite are present but in smaller quantities. Phyllosilicates contents fluctuate slightly around 50% throughout the section but decrease significantly under 20% between 160 and 220 m (CNE 12/CNE 13 zones) and 320–340-m, just above the Zaghouan chert beds interval. Relatively high quartz contents are observed in the basal part of the section (0–60 m, 30%) and decrease rapidly to 10% between 60 and 220 m. Quartz contents highly fluctuate from 10 to 40% in the 220–380 m interval, including the cherts interval, and decrease gradually to 10% toward the top of the section. Inversely calcite contents are very low (close to 0%) in the same interval encompassing the Zaghouan chert beds interval, and quite elevated (up to 40%) at the base (0–220 m) and toward the top (380–580 m) of the section. Gypsum exhibits significant peaks (40–70%) between 160 and 360-m. K-felspar (0–12%) shows no significant trends but the plagioclase content (1–7%) gradually increases from 200 m to the top of the section (Fig. 6). Secondary minerals such as dolomite (0–6%), goethite (0–6%), and ankerite (0–2%), gradually increase from 200 m up to the top of the section. Pyrite (0–2%) seems more abundant in the 100–220-m interval. A detrital index (DI) is calculated by dividing the sum of quartz, feldspar, plagioclase, and phyllosilicates contents by calcite (e.g., Adatte et al., 2002; Bomou et al., 2013). High DI values suggest an important delivery of terrigenous material from continental sources or dilution by carbonate inputs. At the Souar section, a significant increase of DI is observed at the Lutetian–Bartonian boundary (Amami-Hamdi et al., 2016; Ben-Ismail-Lattrache, 2000; Ben-Ismail-Lattrache et al., 2014; Jovane et al., 2010) with a maximum in the Zaghouan chert beds interval. Below and above this interval, DI is close to 0, except for some peaks respectively located at 30, 200, 500, and 570 m (Fig. 6).

3.5. Detrital proxies, calcium carbonate, and biogenic silica

Three paleoenvironmental proxies were selected for paleoenvironmental reconstruction: Titanium (Ti) and Aluminium (Al) which are used to examine changes in terrestrial flux. We used the recalculated % $CaCO_3$ with the abundance of calcareous nannofossils (N/mm^2) to estimate the biogenic calcium carbonate. The relative abundance of radiolarians with Si, Si/Ti, and Si/Al are used to discuss the biogenic silica versus detrital input origin of the high Si content observed in the Djebel Zaghouan Mb. Trends in each of the proxies are discussed in detail in the following sections. The shapes of Si, Si/Ti, and Si/Al curves (Fig. 3) all follow the same trends with an overall negative correlation between these elements and the recalculated $CaCO_3$ content. A clear decreasing trend in Titanium is observed from the bottom of the section up to the Bartonian-Priabonian boundary. The lowest values in Ti occur between

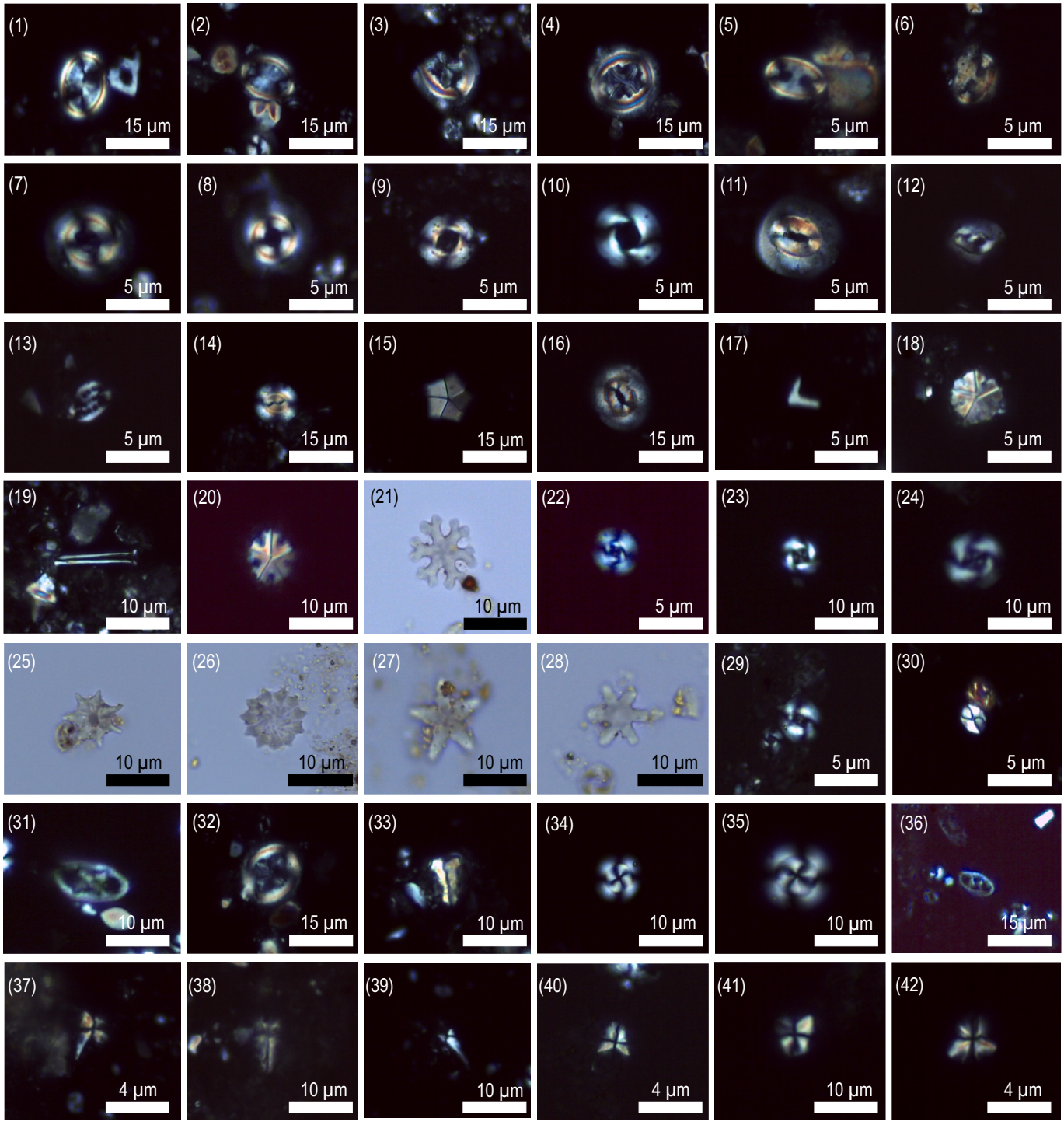

Fig. 4. Photomicrographs of selected calcareous nannofossils. The scale is indicated at the bottom of the plate. 1. *Pontosphaera versa*. CNE 12 Zone. Sample n°: 17. 2. *Reticulofenestra oamaruensis*. CNE 18 Zone. Sample n°: 55. 3.4. *Chiasmolithus grandis*. CNE 14 Zone. Sample n°: 27. 5.6. *Pontosphaera duocava*. CNE 15 Zone. Sample n°: 33. 7. *Coccolithus formosus*. CNE 15 Zone. Sample n°: 36. 8. *Cyclicargolithus abisectus*. CNE 18 Zone. Sample n°: 55. 9.10. *Reticulofenestra dictyoda*. CNE 18 Zone. Sample n°: 56. 11. *C. pelagicus*. CNE 12 Zone. Sample n°: 18. *12. Helicospaera bramlettei. CNE 15 Zone. Sample n°: 31*. 13. *Pontosphaera multipora*. CNE17 Zone. Sample n°: 46. 14. *Reticulofenestra scrippsae*. CNE17 Zone. Sample n°: 52. 15. *Braarudosphaera perampla* (13 µm). CNE14 Zone. Sample n°: 26 16. *Coccolithus eopelagicus*. CNE 15 Zone. Sample n°: 35. 17. *Micrantholithus astrum*. CNE 14 Zone. Sample n°: 26. 18. *Pemma basquensis*. CNE 14 Zone. Sample n°: 27. 19. *Blackites spinosus*. CNE12 Zone. Sample n°: 18. 20. *Pemma basquensis*. CNE 14 Zone. Sample n°: 27. 21. *Discoaster deflandrei*. CNE15 Zone. Sample n°: 35. 22. *Cyclicargolithus floridanus*. CNE17 Zone. Sample n°: 51. *23. 24. Reticulofenestra reticulata* (*C. reticulatum*). *CNE 15 Zone. Sample n°: 36*. 25. *Discoaster saipanensis*. CNE18 Zone. Sample n°: 59. 26. *Discoaster barbadiensis*. CNE18 Zone. Sample n°:56. 27. *Discoaster tanii*. Variety 1 (12 µm). CNE17 Zone. Sample n°: 47. *28. Discoaster nodifier*. CNE14 Zone. Sample n°: 29. 29. *Reticulofenestra lockerii*. CNE18 Zone. Sample n°: 5. 30. *Lanthernitus minutus*. CNE17 Zone. Sample n°: 50. 31. *Campylosphaera dela*. CNE 13 Zone. Sample n°: 20. 32. *Chiasmolithus gigas*. CNE 10/11 Zone. Sample n°: 7. 33. *Braarudosphaera stylifera*. CNE15 Zone. Sample n°: 51. 34. 35. *Reticulofenestra erbae*. CNE 17 Zone. Sample n°49. 36. *Neococcolithes dubius*. CNE 15 Zone. Sample n°: 35. 37. *Sphenolithus kempii*. CNE10/11 Zone. Sample n°: 10. 38. *Sphenolithus radians*. CNE 12 Zone. Sample n°: 16. 39. *Sphenolithus obtusus*. CNE 15 Zone. Sample n°: 35. 40. 41. *Sphenolithus moriformis*. CNE 17 Zone. Sample n°: 5. 42. *Sphenolithus spiniger*. Souar section (CNE 14 Zone). Sample n°: 25.

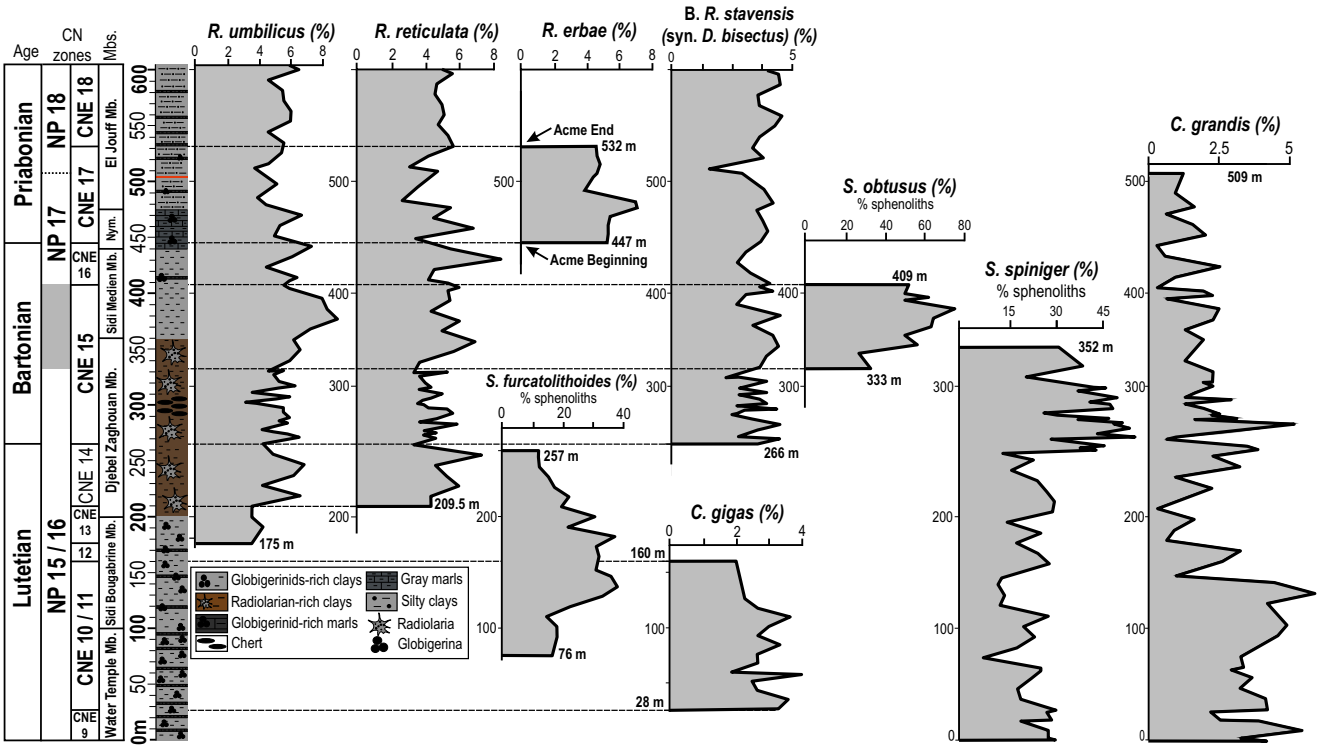

Fig. 5. Abundance patterns of the index CN species are used for middle-Late Eocene biostratigraphy (Agnini et al., 2014). The X-axis values represent the percentages relative to 300 counted specimens, except for *sphenoliths* where the percentages are relative to all *sphenoliths* as in Fornaciari et al. (2010) and (Agnini et al., 2014).

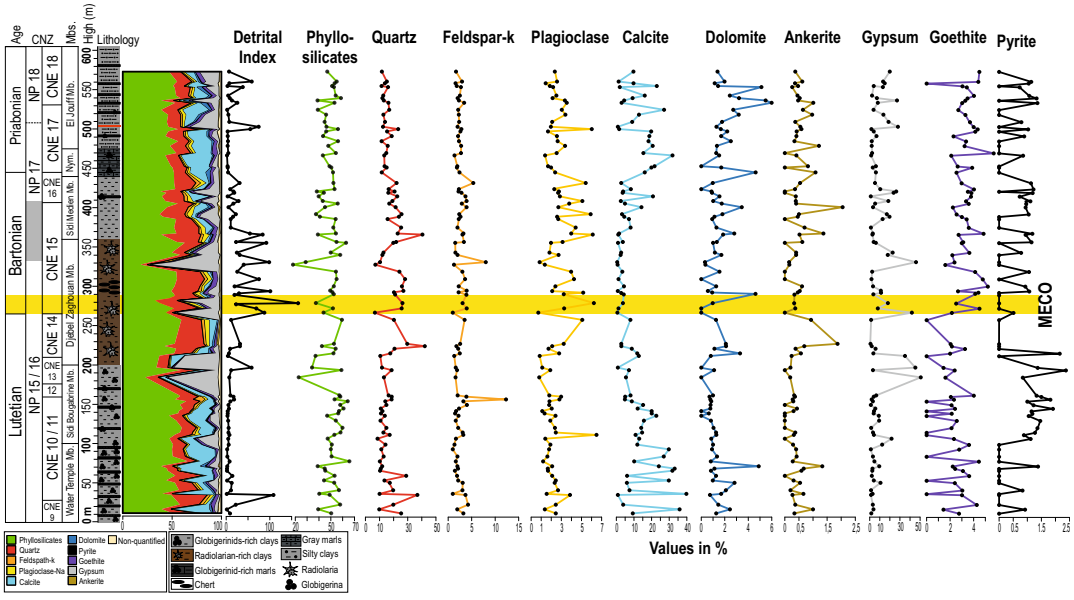

Fig. 6. Bulk mineralogy data (XRD) of the Souar section with the abundance of phyllosilicates, quartz, feldspar-k, plagioclase, calcite, dolomite, ankerite, gypsum, goethite, pyrite, and overall detrital index throughout the section. The early Bartonian coincides with a peak in the detrital index followed by high values during the late Bartonian then a return to low values in the Priabonian deposits.

200 m to 440 m (i.e., CNE13 to CNE16): 49 to 53 ppm between 200 and 300 m and 45 to 51 ppm between 300 and 440 m. The highest Ti values are observed in the early Priabonian (up to 55 ppm). The Priabonian argillaceous marl of Les Nymphes Mb. shows the maximum content in Ti that correlates with low CaCO3 values (less than 30%).

The Aluminium reveals increased values in the lower (CNE9 to CNE13) and upper (CNE17 to CNE18) parts (Fig. 3). Trends in Al appear of lower amplitude variations than other elements. The curve starts with low values in the first 80 m. Between 80 m and 440 m values are stable and vary between 540 and 620 ppm. The Priabonian deposits show the highest Al values recorded with a maximum of 626 ppm at 520 m within the El Jouff Mb.

Si, Si/Al, and Si/Ti show essentially the same trends. Low values in the three proxies dominate the Water Temple and the Sidi Bougabrine Mbs. with a slow increase that ends with a local maximum in the three proxies near the 200 m level. Elevated values dominate the Djebel Zaghouan and the Sidi Medien Mbs. (200 to 440-m). Absolute maxima in Si, Si/Ti, and Si/Al are detected within the Zaghouan chert beds where

also an absolute minimum in Ti, $CaCO_3$, and total nannofossil abundance in N/mm^2 occur. The observed high values in Si, Si/Ti, and Si/Al together with our observation of the occurrence of radiolarian-rich deposits of the Djebel Zaghouan Mb. and decrease in absolute abundance of calcareous nannofossils suggest that the proxies indicate enhanced in situ biosiliceous production taking over pelagic carbonate production. The basal Priabonian deposits of the Les Nymphes Mb. show a drastic decrease in Si and Si/Al together with a drop of radiolarians and return to significantly higher carbonate values suggesting the complete end of biosiliceous production (Fig. 3).

Different trends are observed in the Si, Al, and Ti curves that could be related to the relative contribution of biogenic silica (BSi), silts, and other detrital aluminosilicates. While Al is present in all aluminosilicates, hence in clays, Ti is present both in clays and in the silt fraction under the form of oxides and magnetic minerals. The significant increase in Ti preceded the obvious enrichment in silt in the sediments of the El Jouff Mb. and marks a significant increase in the detrital fraction during the Priabonian.

The Lutetian-Bartonian boundary is immediately followed by the occurrence of the Zaghouan chert beds. This horizon shows a global minimum in Ti and $CaCO_3$ concentrations, as well as a global maximum in Si/Ti, Si, and $\delta^{13}C_{org}$. The Bartonian-Priabonian boundary (~440 m) placed within the lower Les Nymphes Mb., shows a distinct response in our proxies with a sharp positive shift in the recalculated $CaCO_3$ content and the CN abundance, a distinct positive shift in Ti, negative shift in Si, Si/Ti, and Si/Al (Fig. 3).

3.6. Bulk organics carbon isotopes

Stratigraphic values of $\delta^{13}C_{org}$ are plotted in Fig. 7. Values range between −25‰ and − 22.5‰ VPDB, and most samples are around −23‰ organic carbon. The profile shows higher values in the first 100 m (−23‰ VPDB) followed by depleted values around −25‰ from 120 to 150 m. Above 150 m, a long-term increasing trend is observed until a maximum of −22.5‰ is reached at 290 m (the base of the Zaghouan chert beds). But this maximum is preceded by a sharp and short-lived negative excursion with minimal values reaching −24.66‰ at 288 m. Immediately above the positive excursion at 290 m, we record a decreasing trend between 290-m and 390-m, and primarily depleted values down to −25‰ in the late Bartonian. Values return to ca. -24‰ and fluctuate back and forth around this average of −24‰ in the early Priabonian while a more distinct low is observed in our topmost analysed samples with values reaching down to −25‰ again in the Priabonian El Jouff Mb (Fig. 7).

4. Discussion

4.1. Age framework from planktonic foraminifera

From a chronostratigraphic perspective, Burollet (1956) dated the Souar Formation units by their micro-faunal content. The foraminiferal assemblage composition of the Souar section is typical of subtropical to temperate climate dominated by the *Globigerinatheka* group (Dalbiez, 1955; Burollet, 1956; Bonnefous and Bismuth, 1982; Ben-Ismail-Lattrache and Bobier, 1984). The *Clavulinoides* I zone of units 1 and 2 of Burollet (1956) contains the following assemblage: *Pseudoglandulina*,

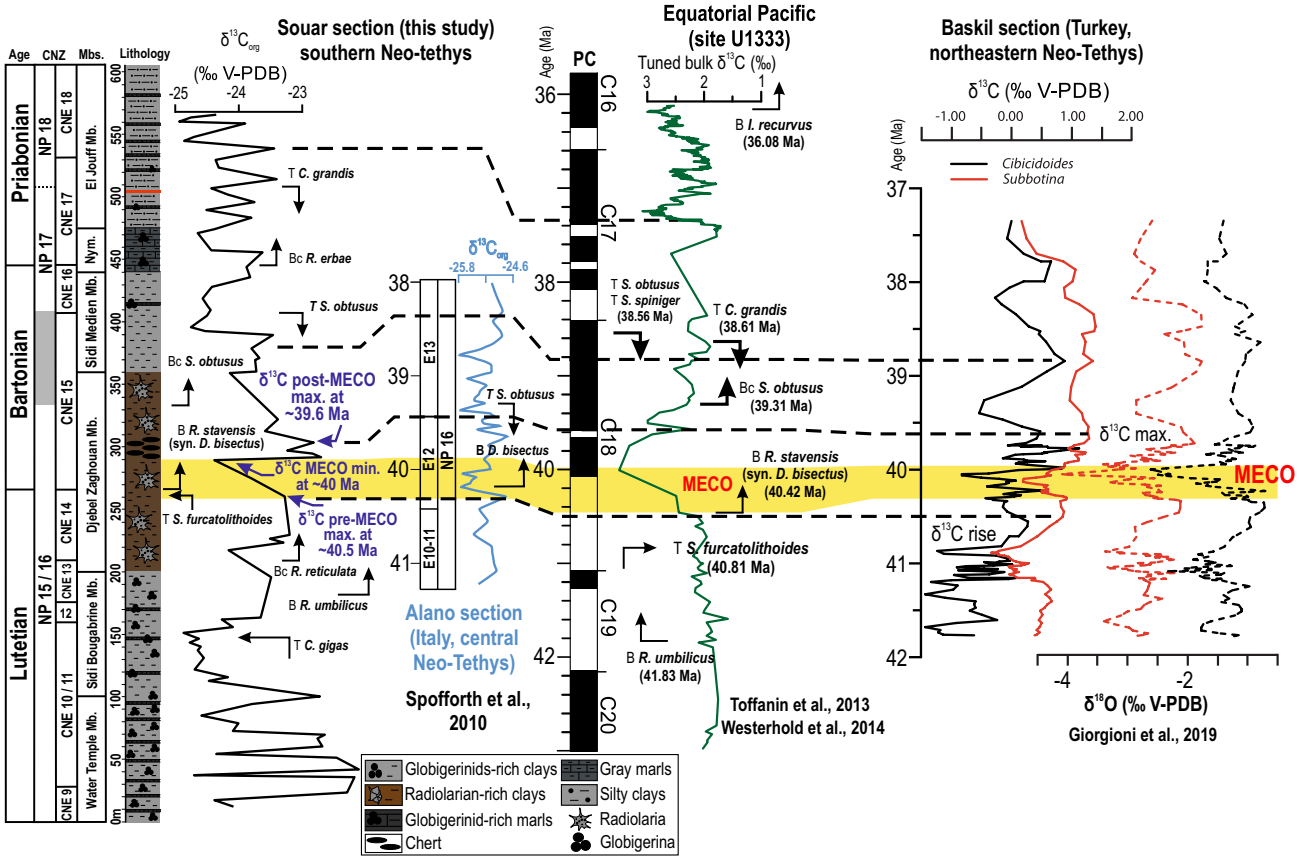

Fig. 7. Proposed correlation of our $\delta^{13}C_{org}$ curve to the $\delta^{13}C_{org}$ curve in the Alano section (Italy, Spofforth et al., 2010), to the astronomically calibrated carbon isotope curve with main calcareous nannofossils horizons from the Pacific (U1333, Toffanin et al., 2013; Westerhold et al., 2014), and the stable isotopes curves of the Baskil section (Turkey, Giorgioni et al., 2019). For the Baskil section, $\delta^{13}C$ and $\delta^{18}O$ isotopes are shown for the thermocline (*Subbotina*) and bottom-water (*Cibicidoides*) conditions.

Globigernia, *Bulimina* sp., *Uvigerina gardnerae, Massilina decorata, Spiroplectammina, Globorotalites, Clavulinoides, Globigerinoides, Eponides cocoaensis, Lenticulina, Cassidulina globosa*, and *Hantkenina dumblei* that indicate the transition from the early to the late Lutetian. The Burollet (1956) *Bulimina* 101 Zone of unit 3 and unit 4 contains *Globigerina topilensis, G. bulloides-cryptomphala*, and *Hantkenina alabamensis, Uvigerina, Bolivina, Lenticulina*, *lenticulina, Globigerinoides mexicanus*, and *Pseudoglandulina* (Burollet, 1956). That fauna, with *Globigerinoides mexicanus*, would indicate the transition from the middle to the Late Eocene (Coxall, 2000). A comparison has been performed between the Souar section and the Cap Bon section (NE Tunisia) where Ben-Ismail-Lattrache, 1981 and Ben-Ismail-Lattrache and Bobier, 1984 provided a detailed PF zonation of the middle-Late Eocene succession, allowing for a correlation of the Souar section to the Cap Bon succession (Fig. 8).

4.2. Age-depth model

To build our Bayesian Bacon age-depth model, we have compiled

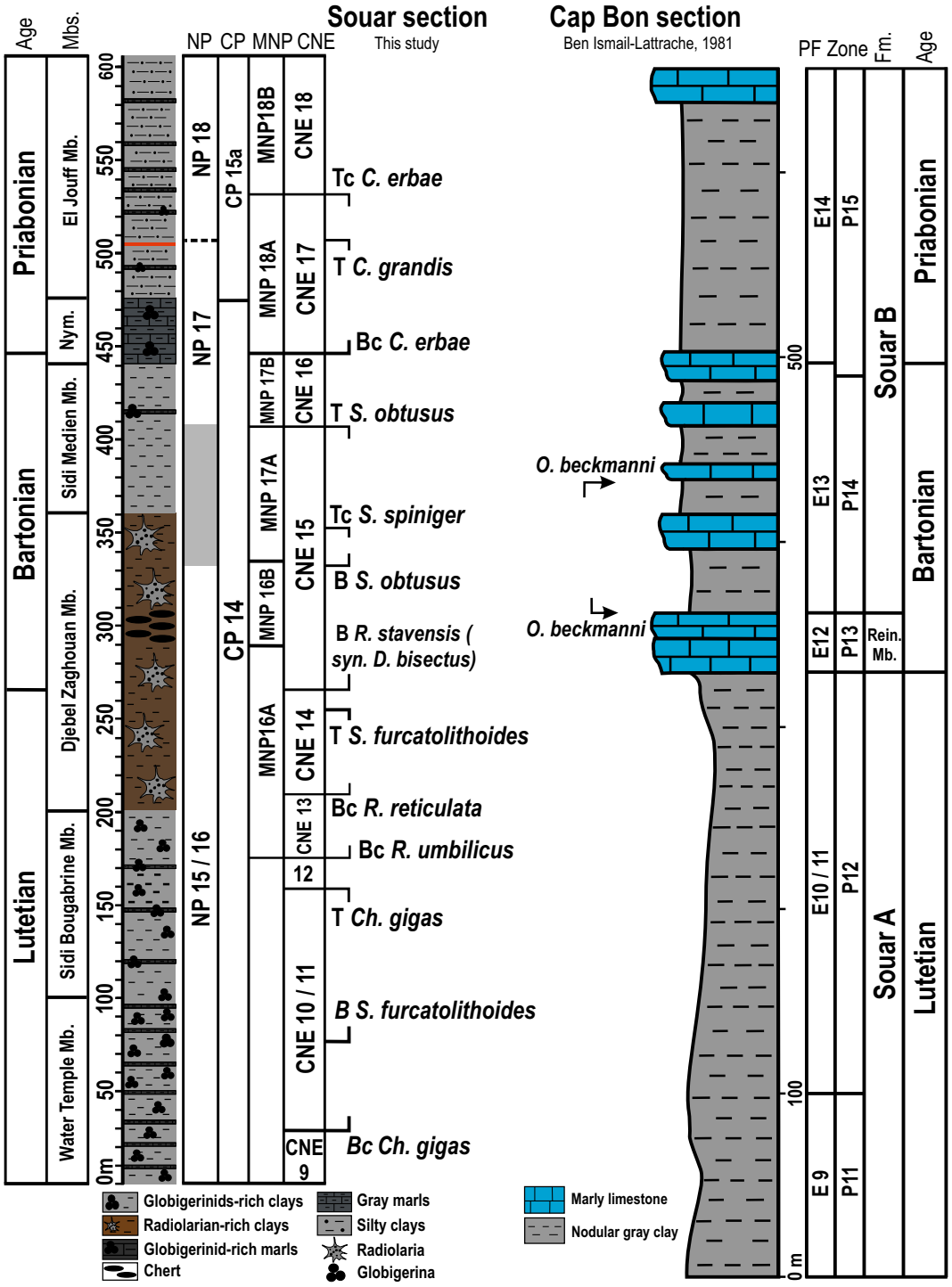

Fig. 8. Litho-bio- and the chronostratigraphic comparison between the Souar section and the Cap Bon (NE Tunisia, Ben-Ismail-Lattrache, 1981; Ben-Ismail-Lattrache and Bobier, 1984). There is no obvious hiatus in the Cap Bon section. Note that the Reneiche member is absent in the Souar section, where instead of carbonate sedimentation, silty clays and glauconitic sandstones characterize the latest Lutetian to early Bartonian.

numerous well-calibrated nannofossil events and recognizable carbon-isotope events in Table 1. For nannofossil events, we have provided the median, minimum, maximum, and average age with uncertainty from this compilation. Often, a majority of the ages given for one bio-horizon agree well within ±200 kyr while one or two ages show more discrepancy >500 kyr (Table 1). A significant difference between the median and average pointed toward some outlying ages that likely have a negative influence on a calculated average. For two bio-horizons, we discarded such outliers and rather chose to make a selection of the most probable ages to calculate an average and uncertainty (see all details in the caption of Table 1).

Age estimates derived from the Bacon model based on the calcareous nannofossil biostratigraphy of the Souar section are reported in the age-depth model (Fig. 9). In this model, the average age may not perfectly align with the biozone boundaries that were drawn on the occurrence event and not on the average. We added the position of the MECO and Late Eocene warming event. The MECO corresponds to E405 cycle 100 (or Eo-C18r, Wade et al., 2011; Westerhold and Rohl, 2013) and thus takes place between 40.48 and 39.94 myr while considering its calibration to astronomical solution La2010b (Westerhold and Rohl, 2013). The age of the Late Eocene warming event is that given in Bohaty and Zachos (2003) and Agnini et al. (2011). Also, the correlation of our carbon isotope curve on organics to that of benthic foraminifer carbon isotope curves of astronomically calibrated Atlantic and Pacific deep-sea sites, supported by the nannofossil biostratigraphy, suggests the identification in our record of three isotopic events previously used to identify the MECO (Boscolo Galazzo et al., 2014; Savian et al., 2014; Khanolkar et al., 2017; Giorgioni et al., 2019): the $\delta^{13}C$ pre-MECO maximum at ~40.5 Ma, the $\delta^{13}C$ MECO minimum at ~40 Ma, followed by a $\delta^{13}C$ post-MECO local maximum as well as a potential $\delta^{13}C$ maximum at ~37.4 Ma. These ages are thus reported on our age-depth plot and further come in support of the age model.

Subsequently, the gray envelope of uncertainty and favored line of correlation is given by the Bacon model and allows us to derive average sedimentation rates (in red on Fig. 9). An extreme reduction of sedimentation rate was suggested in our dataset between T *C. gigas* and Bc *R. umbilicus* (Zone CNE12) before the application of the Bacon model, which supports strong condensation or a hiatus. The markers for CNE11 were not identified in our study and the defining events for the base and top of CNE12 both lie pretty close to the suggested hiatus. Despite having increased the sampling resolution for nannofossil biostratigraphy in this interval, we note a restricted interval of 15 m for CNE12, generally characterized by worsened preservation of the calcareous nannofossil assemblage, possibly increasing the uncertainty bound to the position of the two-defining bio-events for this zone. Hence, we have favored running a Bacon model with a potential hiatus which was set for a maximum duration of 1 myr while the model output, suggests a hiatus of precisely 0.77 myr truncating most of the Lutetian CNE12 zone (Fig. 9). This hiatus is further supported by several authors who reported potential hiatus near the Lutetian–Bartonian of central Tunisia (Ben Ismail-Lattrache, 2000; Jorry, 2004). Surprisingly, our age model does not support a hiatus in the lower CNE15 zone, albeit characterized by glauconitic chert of the Zaghouan chert beds (unit 2) that may be associated with condensation. We notice, however, that according to our age model, the sedimentation rate immediately increases by ca. x1.5 in the upper Djebel Zaghouan Mb. so this level is in any case associated with a change in the flux of sediment to the basin that postdates the MECO (Fig. 9).

4.3. Palaeoproductivity and silica source

Analysis of bulk silicon variability as a proxy for biogenic silica (BSi) is complicated by the fact that Si is also derived from detrital sources (DSi). Elemental ratios of Si by robust detrital components such as Ti or Al have been used in combination with Si to highlight the potential opposition between biosiliceous production and detrital input (e.g., Ragueneau et al., 2005; Nieto-Moreno et al., 2011; Ver Straeten et al., 2011; Kylander et al., 2013). If the variations in Si, Si/Ti, and Si/Al ratios indicate changes in the relative contribution of detrital input, variability in these three proxies will be close to the variations in the detrital proxies (Ti, and Al). Comparison between the used proxies allows us to identify those trends in Si, Si/Ti, and Si/Al proxies are not coupled to changes in detrital proxies (paragraph 3.3 and Fig. 3). We propose that this is due to the enhanced BSi especially within the interval of obvious radiolarian-rich deposits highlighted in Fig. 3. This interval coincides with an increased abundance of siliceous microfossils (radiolarians but also possibly other biosiliceous organisms) and the occurrence of cherts strengthening our assumption of an enhanced BSi production during the middle Eocene (e.g., Henchiri and Slim-S'himi, 2006; Tlig et al., 2010).

Continental weathering is also a major source of Si for radiolarians to build their tests which imply episodic periods of enhanced detrital flux across the Lutetian-Bartonian transition in the Tunisian dorsal (Ben-Ismail-Lattrache, 1981; Ben-Ismail-Lattrache and Bobier, 1984). The detrital input to the Tunisian dorsal is ascribed to a volcanic province (e.g., Clocchiatti and Sassi, 1972; Zaïer et al., 1998; Beji-Sassi et al., 2001; Henchiri and Slim-S'himi, 2006; Henchiri, 2007) and the very low carbonate content observed in the late Lutetian to the late Bartonian

Table. 1
Position of the identified calcareous nannofossils biohorizons at the Souar section and age estimations from the literature. In blue: these ages correspond to the Base of these events, not to their Bc. In red: these ages have not been taken into account in the calculation of the average age used in our Bacon model. For B *R. stavensis*, the age obtained at ODP Site 711 looks like an outlier as compared to all other ages that agree well with each other. For T *C. grandis*, two families of distinct ages can be distinguished for this taxon, we chose to consider only the ages that are in accordance with its extinction in the Tethys.

This study			Jovane et al. (2010)	Toffanin et al. (2013)	Fioroni et al., (2015)	Rodelli et al. (2018)	Luciani et al. (2020)	Luciani et al. (2020)	Agnini et al. (2014)	Westerhold et al. (2020)	Agnini et al. (2014)	Fornaciari et al. (2010)	Fornaciari et al. (2010)	Boulila et al. (2018)		Median	Min	Max	Average	error
Biohorizons	Height (m)	Uncertainty (m)	Contessa	IODP Site U1333	ODP Site 711	Baskil (Turkey)	Alano	Varignano	Massignano	ODP Site 1263	ODP Site 1051	ODP Site 1052	ODP Site 1263	IODP U1408A	IODP U1410	ka	ka	ka	ka	kyr
Tc R. erbae	532	9			36920	37400	37496	37417	37417		37460	37261				37417	36920	37496	37208	144
T C. grandis	509	14.5		**38612**	37570	37200	37780	37610	37610	**38930**	37770	37527		**38532**	**39072**	37770	37200	37780	37490	290
Bc R. erbae	447	9.5			38030	37900	37892	37866	37866		37880	37624				37880	37624	38030	37827	102
T S. obtusus	409	9.5		38562	37780	39500	38289	38353	38353		38470	38229				38353	37780	39500	38640	430
T./Tc S. spiniger	352	5.9		38562		39700	39604									39604	38562	39700	39131	285
Bc S. obtusus	333	9		39314	39000	39500	39604	39758	39758			39827	39224			39552	39000	39827	39414	207
B R. stavensis (syn. D. bisectus)	266	3		40421	**39000**	40100	40525	40298	40298	40080	40340	40354	40294	40270	40070	40296	40070	40525	40298	114
T S. furcatolithoides	257	6	40510	40814	40170	41100	40708	40502	40502		40510		40533		40290	40510	40170	41100	40635	233
Bc R. reticulata	209.5	9.5			41330	41200	41033				42370			**42660**	**42680**	41850	41033	42680	41857	412
Bc R. umbilicus	175	9.5	42670	41829	42670					42480	43060			**44100**	**43880**	42670	41829	44100	42965	568
T C. gigas	160	13								44160	43960			45140	44520	44340	43960	45140	44550	295
B S. furcatolithoides	76	9.5									45950			45900	45410	45900	45410	45950	45680	135
B C. gigas	28	2								45240	46110			46300	46170	46140	45240	46300	45770	265

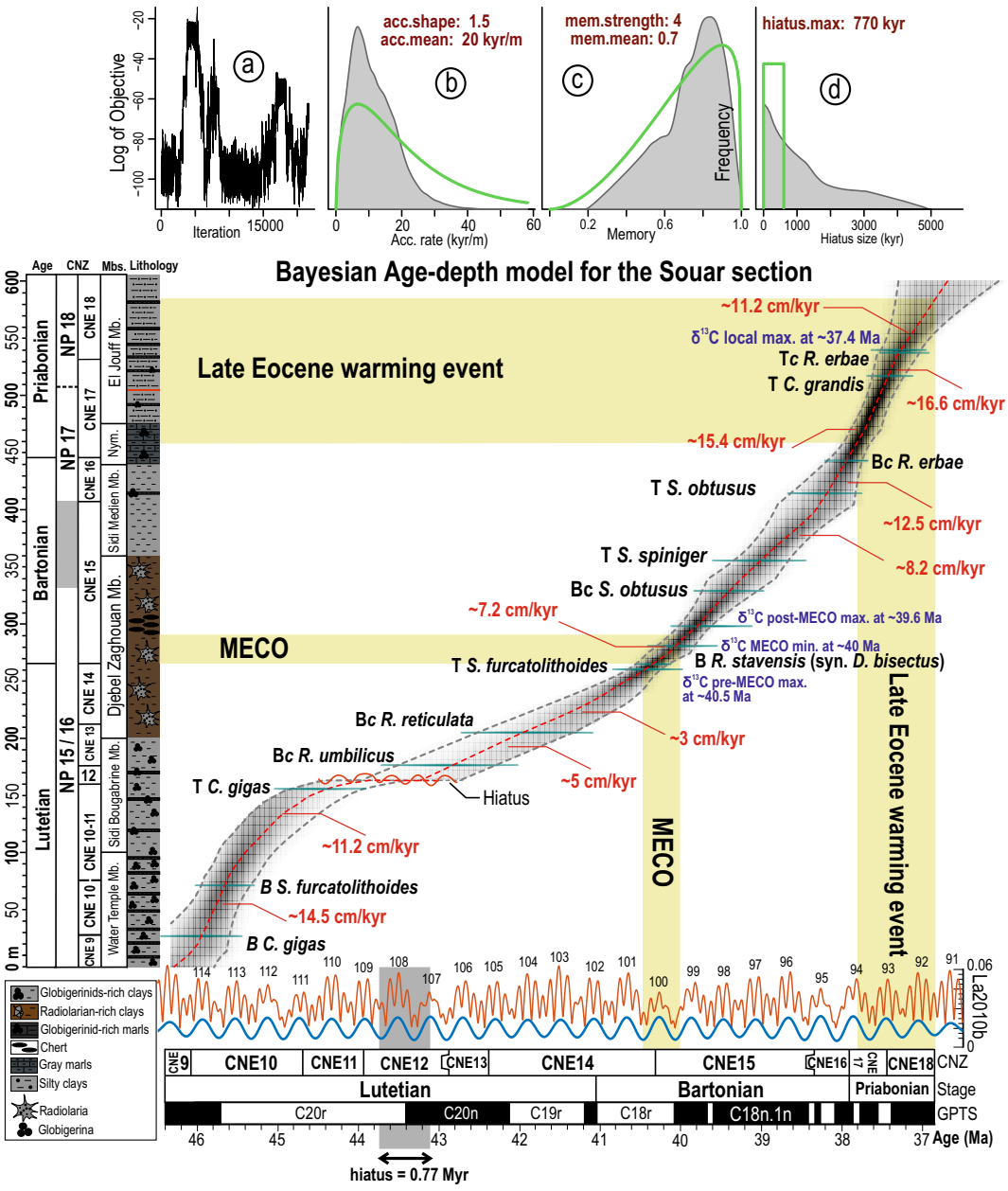

Fig. 9. Stratigraphy and Bayesian age-depth modelling for the Souar section from Lutetian to Priabonian Stages (Global Timescale after Ogg et al., 2016) with a hiatus within the CNE12 zone. Bayesian Bacon age-depth model (Bchron, http://cran.r-project.org/web/packages/Bchron/index.html) based on biostratigraphic markers (Table 1) and organic carbon isotopes events. Gray-scales indicate all possible age-depth models, dotted lines indicate the mean and 95% confidence ranges, red dashed line is the mean. Biostratigraphic markers are plotted as horizontal bars representing uncertainty ranges. The rock accumulation rates are indicated in cm/kyr. The top graphs display the MCMC (Markov chain Monte Carlo) run (a), the prior (green curve), and the posterior (gray-filled curve) distributions for accumulation rate (b), variability/memory (c), and hiatus size (d). The MECO corresponds to cycle 100 Eo-C18r (Wade et al., 2011; Westerhold and Rohl, 2013). (For interpretation of the references to colour in this figure legend, the reader is referred to the web version of this article.)

sediments of the Souar Formation preclude that any detrital input was sourced from the NE and SW carbonates shelves where the nummulitic-rich carbonates of the Reneiche /Siouf member were concomitantly deposited.

4.4. *Bartonian and Priabonian definition and the Tunisian account*

The biostratigraphy of the middle-Late Eocene in Tunisia has been the subject of several low-resolution studies, leading to disagreement on the position of most of its stages (Burollet, 1956; Bismuth and Bonnefous, 1981; Bonnefous and Bismuth, 1982). Our age-depth model constitutes a significant improvement and the correlation of the Souar section to sections in the NE carbonate platform and the SW of central Tunisia dated by foraminifers and ostracods (Fig. 10) allows for the construction of a new comprehensive stratigraphic chart for the middle-Late Eocene of Tunisia (Fig. 11). Our section spans the Lutetian/Bartonian and Bartonian/Priabonian boundaries. None of these two-stage boundaries have yet been ratified by the International Commission on Stratigraphy (ICS). The base Bartonian has been suggested to be positioned at the base of magnetochron C18r (Ogg et al., 2008) and near the Tc of *R. reticulata,* which defines the base of CNE14 (Agnini et al., 2014) but there are other potential criteria such as the base of the very short Chron C19n and top of *R. umbilicus* (>14 μm). For PF, the base of *O. beckmanni* that defines the base of zone E12 would constitute an excellent deep-sea biostratigraphic

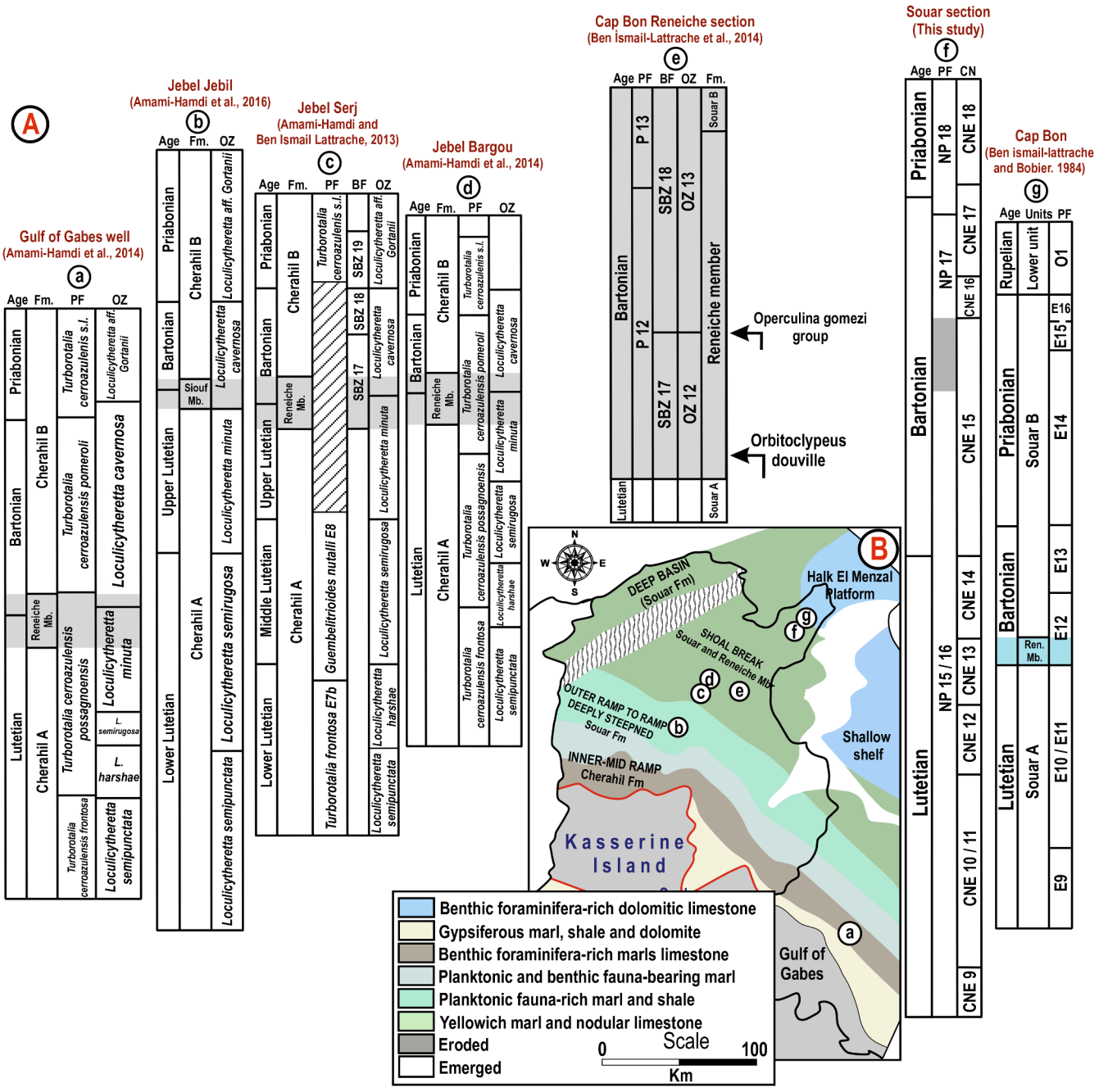

Fig. 10. (A) A summary of previous studies on the middle-Late Eocene series in Tunisia. (B) Middle-Late Eocene paleogeography and facies map (Fakhfakh Ben Jemai, 2001) with the location of the previous works: (a) Gulf of Gabes (Amami-Hamdi et al., 2014); (b) Jebel Jebil (Amami-Hamdi et al., 2016); (c) Jebel Serdj (Amami Hamdi and Ben Ismail Lattrache, 2013); (d) Jebel Bargou (Amami-Hamdi et al., 2014); (e) Cap Bon (Ben-Ismail-Lattrache and Bobier, 1984); (f) Souar section; (g) Cap Bon section (Ben-Ismail-Lattrache et al., 2014).

marker but it lies much above the level of the considered chron reversals. Other PF events that have been considered are the base of *T. pomeroli* and *G. euganea* and the top of *G. nuttali* and *M. bandyi*, though the two latter bioevents would then also be positioned much below the favored level of chron reversal (Payros et al., 2015). The base of the Barton Clay Formation, which is the historical stage stratotype for the Bartonian, has been recently demonstrated to be situated a few meters below the base of Chron C18r and within Chron C19n (Hooker and King, 2019). Hence, a position at the base of C18r should theoretically be favored (Hooker and King, 2019). Curry (1981) originally proposed to define the base of the Bartonian in the Barton Clay Formation at the *Nummulites prestwichianus* bed, which has been shown to lie very close to the top of the nannofossil *S. furcatolithoides* (Hooker and King, 2019). This would position a new favored level for the base Bartonian within the base of CNE15. Finally, it is important to precise that for Tethyan and peri-Tethyan large benthic foraminifera (LBF), the base of the Bartonian is situated at the base of SBZ17 (e.g., Özcan et al., 2019; Serra-Kiel et al., 1998) which contains, among numerous species, one species of nummulite that is only characteristic of this zone, *Nummulites perforatus*, and one that first occurs in this zone and ranges up to SBZ18, *Nummulites ptukhiani* (Serra-Kiel et al., 1998).

The correlation of the base of SBZ17 to the base Bartonian of our studied locality, in its strict definition of base *N. prestwichianus* in the English stratotype, is confirmed by the co-occurrence of both *N. prestwichianus* and

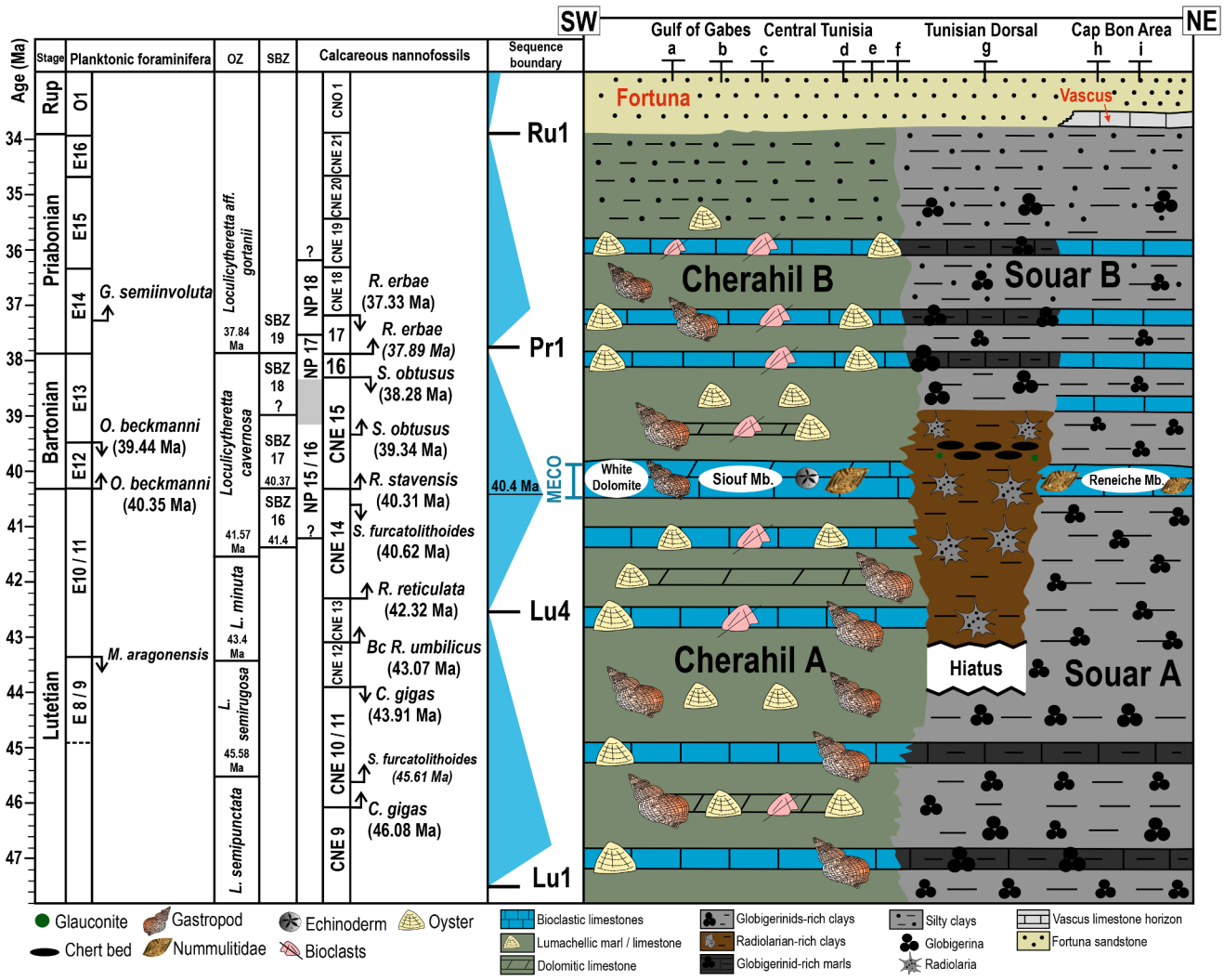

Fig. 11. Stratigraphic chart of the Eocene in central and north-eastern Tunisia. (a) Gulf of Gabes (Amami-Hamdi et al., 2014); (b) Jebel Jebil (Amami-Hamdi et al., 2016); (c) Jebel Serdj (Amami Hamdi and Ben Ismail Lattrache, 2013); (d) Jebel Bargou (Amami-Hamdi et al., 2014); (f) Souar section; (e) Cap Bon (Ben-Ismail-Lattrache and Bobier, 1984); (g) Cap Bon section (Ben-Ismail-Lattrache et al., 2014). The correlation between ostracod, PF, and CN zones allows us to give the exact ages for zones boundaries. Note that the Zaghouan chert beds are younger than the Siouf / Reneiche members and occur after the MECO. The MECO warming coincides with a transient increase in large benthic foraminifera (i.e., *Nummulites*) during the early Bartonian indicating oligotrophic conditions at the shelves wherein the deep basin deposits of the Tunisian dorsal shows enhanced biosiliceous sedimentation attributed to strengthened upwelling regimes.

N. perforatus in certain parts of the Kuma Fm. (Crimean-Caucasus region). In Tunisia, the base occurrence of the Reneiche member and its lateral equivalent in the SW of the Tunisian dorsal, the Siouf member, has been considered as a sharp lithostratigraphic marker for the base of the Bartonian (Ben-Ismail-Lattrache et al., 2014, Figs. 10 and 11), due to the co-occurrence of LBF species *N. ptukhiani* in these beds at the inner platform facies (Amami Hamdi and Ben Ismail Lattrache, 2013) and of a PF assemblage characteristic of the upper P12 zone (Berggren et al., 1995), equivalent to zone E11 (Berggren and Pearson, 2005), described in several sections of outer platform facies by Ben Ismail-Lattrache (2000). In addition, the first occurrence of *Orbulinoides beckmanni,* which defines the base of the E12 zone, is situated either immediately at the top of the Reneiche member or a few meters above (Fig. 11, Ben-Ismail-Lattrache, 1981). The absence of the Reneiche member in the Souar section prevents a clear correlation to our section, though Burollet (1956) considered already that unit 2 was its lateral stratigraphic equivalent. Our age model suggests a slightly younger age for Burollet (1956) Unit 2 with the position of the base Bartonian placed at 270 m (top CNE14), some 20 m below the base of its Unit 2. The definition of the base Priabonian is somewhat better constrained nowadays than that of the Bartonian. The base of nannofossil *Chiasmolithus oamaruensis* which defines the base of NP18 was proposed by Berggren et al. (1995) to approximate this boundary level. However, numerous studies have shown that this species regularly presents discontinuous and sporadic occurrences, and accounts for the diachroneity of its first appearance across latitudes (Agnini et al., 2014; Aljahdali et al., 2020). This criterion has thus been abandoned. The ICS has just agreed upon a definition and upon the erection of a Global Stratotype Section and Point at the base of the Tiziano Bed, a prominent crystal tuff layer at 63.57 m level in the Alano di Piave section, NE Italy (https://timescalefoundation.org/gssp/detail.php?periodid = 27&top_parentid = 0). The primary biostratigraphic markers are the Top of PF *Morozovelloides* and the Base acme of nannofossil *R. erbae*, which occur, respectively, within Chrons C17n.3n and C17n.2n (Luciani et al., 2020). Recent results at the Varignano section (Italy) suggest that this level is situated within SBZ18 for LBF zones, contrary to traditional usage that placed the boundary at the base of SBZ19 (Serra-Kiel et al., 1998). Finally, the Base of PF *G. semiinvoluta* occurs just a few meters above the Bc of *R. erbae* in the Alano and Varignano sections making this species useful to define the Bartonian-Priabonian boundary.

4.5. Contrasts in platform to basin facies across the middle-Late Eocene

Amami-Hamdi et al. (2014) defined the carbonate-rich facies occurring in the Gulf of Gabes well, across the *Loculicytheretta minuta* to *Loculicytheretta cavernosa* Ostracod Zones as the Reneiche member although usually, in the inner part of the ramp, these facies correspond to a distinctive dolomitized limestone defined as the Siouf member which is also observed in the Jebel Jebil section (Figs. 10 and 11). The Reneiche / Siouf member, therefore, appears to correlate strictly from SW to NE across a large range of distinct environments of an intraplatform basin bounded by an SW carbonate ramp and a NE carbonate platform (Fig. 11). However, according to our scheme, none of the two members occur in the Souar section which represents the deepest parts of the basin. The occurrence of the Reneiche / Siouf members precisely at the base of the Bartonian, as dated by planktic and benthic foraminifera in the Cap Bon section (Figs. 10e and 11) suggests that the sudden production of massive, nummulitic carbonate beds was triggered by the climatic conditions leading to and culminating at the MECO Event on the SW carbonate ramp and NE carbonate platform. This shallow-water carbonate maximum triggered by the MECO in the SW and NE of the Tunisian dorsal corresponds however to a carbonate minimum in the Souar Formation that represents the deepest parts of the Basin.

Our age-model and correlation advocates for this contrasting deposition of radiolarian-rich clays in the Souar section during the MECO interval which indicate the installment of an upwelling zone (e.g., Henchiri, 2007; Salamy and Zachos, 1999; Witkowski et al., 2012) in the basinal depocenter of the Tunisian dorsal. The source of primarily siliciclastic deposits was likely not derived from the slopes of the SW ramp or NE shelf as such sources would have necessarily brought carbonate debris and micrite to the basin. Together with a lower sedimentation rate and very low absolute abundance of nannofossils during the latest Lutetian to early Bartonian, these inferences suggest that the massive carbonates built up in the SW and NE were not strongly weathered and eroded during the early Bartonian. Such an environment was not particularly favorable for calcareous nannoplankton growth in the center of the Tunisian dorsal basin.

It remains unclear whether an increased detrital flux accompanied the installment of the upwelling zone that led to the deposition of biosilica-rich sediments. An increased detrital flux in this interval would however suggest material derived under hydrolyzing conditions. More humid conditions appear to have characterized the MECO in other parts of the Neo-Tethys such as Turkey (Giorgioni et al., 2019; Rego et al., 2018) so it is not unreasonable to think that the entire interval covered by our radiolarian-rich sediments was deposited under more humid conditions as suggested by the maximum DI values (see paragraph 3.4 and Fig. 6) during the early Bartonian.

4.6. Mineralogical changes associated with the MECO

Bulk-rock mineralogy analyses are commonly used to characterize the lithological composition and are also a powerful tool to reconstruct climatic change and/or sea-level fluctuations (e.g., Adatte et al., 2002; Henchiri and Slim-S'himi, 2006; Moiroud et al., 2012; Cao et al., 2018). In the Souar section, gypsum, dolomite, ankerite, goethite, and pyrite result of secondary authigenesis linked to late diagenetic processes. Secondary gypsum is produced by the reaction of calcium carbonate with acid sulfate from pyrite oxidation (e.g., Ritsema and Groenenberg, 1993; Pirlet et al., 2010; Moon et al., 2013). Under a semi-arid climate, pyrite present in the sediment is weathered by percolating oxygenated groundwaters linked to the variations of the water table. The sulfuric acid produced by pyrite oxidation is therefore neutralized by calcium carbonate in the marls to form secondary gypsum.

The phyllosilicates, quartz, K-felspar, and plagioclases contents reflect the terrigenous influx coming from the continental erosion, and the calcite contents characterize the marine carbonate productivity. At the end of the Lutetian, a significant increase in the detrital index (detritus/calcite ratio) occurred just before the cherts interval and persisted until the early Bartonian at the end of Djebel Zaghouan Mb. (360 m). However, we cannot completely rule out that a non-negligible part of the quartz content from XRD results is probably linked to the amorphous biogenic silica from radiolarians. The same observed trends between quartz and other detritals minerals such as K-felspar and plagioclase support a concomitant increase of detrital quartz across the Djebel Zaghouan Mb. which parallels the increase in abundance of radiolarians. The observed DI increase thus suggests an intensification of continental weathering, consistent with the climatic warming of the MECO. Furthermore, this interval is also marked by an almost absence of calcite and, together with the low CN abundance, suggests a drop in marine carbonate productivity linked to climatic changes and/or a sea-level rise, consistent with the major transgression of the Lutetian-Bartonian boundary. These data are also supported by the first occurrence of *R. stavensis* (syn. *D. bisectus*) characteristic of warmer temperatures and correlatable with the temperature increase recorded in numerous sections during the MECO. The transition from Globigerinid-rich marls to Radiolarian-rich and glauconitic clays facies of the Djebel Zaghouan Mb., characteristic of a deeper environment, is consistent with the Lutetian-Bartonian transgression. This large increase in a terrigenous influx that accompanies the increase in biosiliceous production is even more significant from a climatic perspective as more distal conditions and hence increased distance from the continental detrital source likely occurred in this high sea-level context.

5. Conclusions

A combined calcareous nannofossil biostratigraphic and chemostratigraphic ($\delta^{13}c_{org}$) framework has been used as input for constructing a Bayesian age-depth model and to provide the first high-resolution stratigraphic record of the middle-Late Eocene in the south-western Neo-Tethys (Tunisian dorsal). The studied Souar section extends from 46.29 Ma to 36.69 Ma with high sedimentation rate variations (varying from 4.8 up to 15.8 cm/kyr) and comprises at least one hiatus that accounts for approximately 0.77 Myr and truncates most of zone CNE12. A correlation between the $\delta^{13}C_{org}$ of the Souar section and other published reference sections (Pacific and Neo-Tethys) suggests the identification of the $\delta^{13}C$ pre-MECO local maximum at ~40.5 Ma, of the $\delta^{13}C$ MECO minimum at ~40 Ma, as well as a potential $\delta^{13}C$ maximum at ~37.4 Ma. These correlations, also supported by our calcareous nannofossil biostratigraphy have helped to identify the middle-Late Eocene stage boundaries. According to the correlation of Souar to shelf sections in Tunisia, we confirm the position of the Lutetian-Bartonian boundary within the Reneiche and Siouf members in carbonate platform deposits. The Reneiche and Siouf member appear to correspond to the expression of the warming leading to and culminating at the Middle Eocene Climatic Optimum (MECO) within the lower CNE15 calcareous nannofossil zone (39.9 to 40.4 Ma). Strikingly, we show that while a peak of carbonate production and return to nummulitic production characterized the MECO interval on the NE and SW carbonate platforms, an upwelling zone likely developed in the depocenter of the Tunisian dorsal at the location of the Souar section, as supported by a significant increase in biosiliceous production. The development of this upwelling zone drastically reduced in situ calcareous nannoplankton, carbonate productivity, and triggered the deposition of radiolarian-rich clays from ca. 850 kyr before to 900 kyr after the MECO. This episode of radiolarian-rich clay deposition was accompanied by a significant increase in terrigenous flux to the basin likely related to enhanced hydrolysing conditions triggered by climate warming.

Declaration of competing interest

The authors declare that they have no known competing financial interests or personal relationships that could have appeared to influence the work reported in this paper.

Acknowledgments

Funding for this study was ensured through internal funds from the University of Copenhagen allocated to J.H.M. via the double-degree Ph. D. program. T.A. and N.T. also acknowledge the IGN International Academy program that facilitated collaboration between KU and Lausanne.

Appendix A. Supplementary data

Supplementary data to this article can be found online at https://doi.org/10.1016/j.palaeo.2021.110639.

References

Adatte, T., Stinnesbeck, W., Keller, G., 1996. Lithologic and mineralogic correlations of near K/T boundary clastic sediments in NE Mexico : implication for origin and nature of deposition. Sp. Publ. Soc Geol Am. 307, 211–226. https://doi.org/10.1130/0-8137-2307-8.211.

Adatte, T., Keller, G., Stinnesbeck, W., 2002. Late Cretaceous to early Paleocene climate and sea-level fluctuations: the Tunisian record. Palaeogeogr. Palaeoclimatol. Palaeoecol. 178, 165–196. https://doi.org/10.1016/S0031-0182(01)00395-9.

Agnini, C., Muttoni, G., Kent, D.V., Rio, D., 2006. Eocene biostratigraphy and magnetic stratigraphy from Possagno, Italy: the calcareous nannofossil response to climate variability. Earth Planet. Sci. Lett. 241, 815–830. https://doi.org/10.1016/j.epsl.2005.11.005.

Agnini, C., Fornaciari, E., Giusberti, L., Grandesso, P., Lanci, L., Luciani, V., Muttoni, G., Pälike, H., Rio, D., Spofforth, D.J.A., Stefani, C., 2011. Integrated biomagnetostratigraphy of the Alano section (NE Italy): a proposal for defining the Middle-Late Eocene boundary. Bull. Geol. Soc. Am. 123, 841–872. https://doi.org/10.1130/B30158.1.

Agnini, C., Fornaciari, E., Raffi, I., Catanzariti, R., Pälike, H., Backman, J., Rio, D., 2014. Biozonation and biochronology of Paleogene calcareous nannofossils from low and middle latitudes. Newsl. Stratigr. 47, 131–181. https://doi.org/10.1127/0078-0421/2014/0042.

Ahm, A.-S., Bjerrum, C.J., Hammarlund, E.U., 2017. Disentangling the record of diagenesis, local redox conditions, and global seawater chemistry during the latest Ordovician glaciation. Earth Planet. Sci. Lett. 459, 145–156. https://doi.org/10.1016/j.epsl.2016.09.049.

Aljahdali, M.H., Elhag, M., Mufrreh, Y., Memesh, A., Alsoubhi, S., Zalmout, I.S., 2020. Upper Eocene calcareous nannofossil biostratigraphy: a new preliminary Priabonian record from northern Saudi Arabia. Appl. Ecol. Environ. Res. 18, 5607–5625. https://doi.org/10.15666/aeer/1804_56075625.

Amami Hamdi, A., Ben Ismail Lattrache, K., 2013. Middle to Upper Eocene ostracods and associated foraminifera of the Jebel Serj section (Central Tunisia). Biostratigraphical, paleoecological and paleobiogeographical significanc. Rev. Micropaleontol. 56, 159–174. https://doi.org/10.1016/j.revmic.2013.10.002.

Amami-Hamdi, A., Ben Ismail-Lattrache, K., Dhahri, F., Saïd-Benzarti, R., 2014. Middle to Upper Eocene ostracofauna of Central Tunisia and Pelagian Shelf: examples of Jebel Bargou and the Gabes Gulf. Arab. J. Geosci. 7, 1587–1603. https://doi.org/10.1007/s12517-012-0816-y.

Amami-Hamdi, A., Dhahri, F., Jomaa-Salmouna, D., Ben Ismail-Lattrache, K., Ben Chaabane, N., 2016. Quantative analysis and paleoecology of Middle to Upper Eocene Ostracods from Jebel Jebil, Central Tunisia. Rev. Micropaleontol. 59, 409–424. https://doi.org/10.1016/j.revmic.2016.10.001.

Backman, J., Hermelin, J.O.R., 1986. Morphometry of the Eocene nannofossil Reticulofenestra umbilicus lineage and its biochronological consequences. Palaeogeogr. Palaeoclimatol. Palaeoecol. 57, 103–116. https://doi.org/10.1016/0031-0182(86)90009-X.

Barker, P.F., Burrell, J., 1977. The opening of Drake passage. Mar. Geol. 25, 15–24.

Bedir, M., Tlig, S., Bobier, C., Issaoui, N., 1996. Sequence stratigraphy, basin dynamics, and petroleum geology of Miocene from the eastern Tunisia. Am. Assoc. Pet. Geol 80, 63–81.

Beji-Sassi, A., Laridhi-Ouzaa, N., Zaier, A., Clocchiatti, R., 2001. Paleocene–Early Eocene alkaline volcanic activity in Tunisia phosphatic sediments. Comparison with cretaceous magmatism and geodynamic significance. Les Journees l'ETAP 47–58.

Ben Ayed, N., 1993. Evolution tectonique de l'avant-pays de la chaîne Alpine de Tunisie du debut du Mesozoïque a l'Actuel. In: Ann. Min. Geol. Tunisie n32, p. 296.

Ben Ferjani, A., Burrollet, P.F., Mejri, F., 1990. Petroleum geology of Tunisia. In: Mém. ETAP, Tunis, n°1 194.

Ben Ismail-Lattrache, K., 2000. Précision sur le passage Lutétien-Bartonien dans les depôts éocenes moyens en Tunisie centrale et nord-orientale. Rev. Micropaleontol. 43, 3–16. https://doi.org/10.1016/S0035-1598(00)90060-6.

Ben-Ismail-Lattrache, K., 1981. Etude Micropaleontologique et biostratigraphique des series Paleogene de l'anticlinal du Jebel Abderrahman (Cap Bon, Tunisie Nord orientale). In: Thèse 3eme cycle Univ 165.

Ben-Ismail-Lattrache, K., 2000. Precision on Lutetian-Bartonian passage of Middle Eocene deposits in central and North-Eastern Tunisia. Rev. Micropaleontol. 43, 3–16.

Ben-Ismail-Lattrache, K., Bobier, C., 1984. Sur l'evolution des paleo-environnements marins Paleogenes des bordures occidentales du Detroit Siculo-Tunisien et leurs rapports avec les fluctuations du paleo-ocean mondial. Mar. Geol. 55, 195–217. https://doi.org/10.1016/0025-3227(84)90069-0.

Ben-Ismail-Lattrache, K., Özcan, E., Boukhalfa, K., Saraswati, P.K., Soussi, M., Jovane, L., 2014. Early Bartonian orthophragminids (Foraminiferida) from Reineche Limestone, north African platform, Tunisia: taxonomy and paleobiogeographic implications. Geodin. Acta 26, 94–121. https://doi.org/10.1080/09853111.2013.858950.

Berggren, W.A., Pearson, P.N., 2005. A revised tropical to subtropical Paleogene planktonic foraminiferal zonation. J. Foraminifer. Res. 35, 279–298. https://doi.org/10.2113/35.4.279.

Berggren, W.A., Kent, D.V., Swisher, C.C., Aubry, M.P., 1995. A revised Cenozoic geochronology and chronostratigraphy. In: Berggren, W.A. (Ed.), Geochronology, Time Scales and Global Stratigraphic Correlation. SEPM (Society for Sedimentary Geology) Special Publication, pp. 129–212. https://doi.org/10.2110/pec.95.04.0129.

Bismuth, H., Bonnefous, J., 1981. The biostratigraphy of carbonate deposits of the Middle and Upper Eocene in northeastern off-shore Tunisia. Palaeogeogr. Palaeoclimatol. Palaeoecol. 36, 191–211.

Blaauw, M., Christeny, J.A., 2011. Flexible paleoclimate age-depth models using an autoregressive gamma process. Bayesian Anal. 6, 457–474. https://doi.org/10.1214/11-BA618.

Bohaty, S., Zachos, J., 2003. Significant Southern Ocean warming event in the late-Middle Eocene. Geology 31, 1017–1020. https://doi.org/10.1130/G19800.1.

Bohaty, S.M., Zachos, J.C., Florindo, F., Delaney, M.L., 2009. Coupled greenhouse warming and deep-sea acidification in the Middle Eocene. Paleoceanography 24, 1–16. https://doi.org/10.1029/2008PA001676.

Bomou, B., Adatte, T., Tantawy, A., Mort, H., Fleitmann, D., Huang, Y., Föllmi, K.B., 2013. The expression of the Cenomanian-Turonian oceanic anoxic event in Tibet. Palaeogeogr. Palaeoclimatol. Palaeoecol. 369, 466–481. https://doi.org/10.1016/j.palaeo.2012.11.011.

Bonnefous, J., Bismuth, H., 1982. Les facies carbonates de plate forme de l'éocène moyen et supérieur dans l'offshore tunisien nord- oriental et en mer pélagienne: Implications paléogéographiques et analyse micropaleontologique. In: Bull. Centres Rech. Explor. Prod. Elf- Aquitaine, 6, pp. 337–403.

Boscolo Galazzo, F., Giusberti, L., Luciani, V., Thomas, E., 2013. Paleoenvironmental changes during the Middle Eocene Climatic Optimum (MECO) and its aftermath: the benthic foraminiferal record from the Alano section (NE Italy). Palaeogeogr. Palaeoclimatol. Palaeoecol. 378, 22–35. https://doi.org/10.1016/j.palaeo.2013.03.018.

Boscolo Galazzo, F., Thomas, E., Pagani, M., Warren, C., Luciani, V., Giusberti, L., 2014. The middle Eocene climatic optimum (MECO): a multiproxy record of paleoceanographic changes in the Southeast Atlantic (ODP Site 1263, Walvis Ridge). Paleoceanography 29, 1143–1161. https://doi.org/10.1002/2014PA002670.

Bouaziz, S., Barrier, Soussi, M., Turki, M., Zouari, H., 2002. Tectonic evolution of the northern African margin in Tunisia from paleostress data and sedimentary record. Tectonophysics 357, 227–253. https://doi.org/10.1016/S0040-1951(02)00370-0.

Bown, P.R., 2005. Palaeogene calcareous nannofossils from the Kilwa and Lindi areas of coastal Tanzania (Tanzania Drilling Project 2003-4). J. Nannoplankt. Res. 27, 21–95.

Bown, P.R., Dunkley Jones, T., 2012. Calcareous nannofossils from the Paleogene equatorial Pacific (IODP Expedition 320 Sites U1331-1334). J. Nannoplankt. Res. 32, 3–51.

Brooks, S., Gelman, A., Jones, G., Meng, X.-L., 2011. Handbook of Markov Chain Monte Carlo. CRC Press, Boca Raton, Florida, p. 619.

Bukry, D., 1971. Cenozoic calcareous nannofossils from the Pacific Ocean. Trans. San Diego Soc. Nat. Hist. 16, 303–328.

Burollet, P.F., 1956. Contribution à l'étude stratigraphique de la Tunisie centrale. In: Ann. Mines et geol., Tunis 18.

Burollet, P.F., Ellouz, N., 1986. L'évolution des bassins sédimentaires de la Tunisie Centrale et Orientale. Bull. des Centres Rech. Explor. Elf-Aquitaine 10, 49–68.

Cao, W., Xi, D., Melinte-Dobrinescu, M.C., Jiang, T., Wise, S.W., Wan, X., 2018. Calcareous nannofossil changes linked to climate deterioration during the Paleocene–Eocene thermal maximum in Tarim Basin, NW China. Geosci. Front. 9, 1465–1478. https://doi.org/10.1016/j.gsf.2018.04.002.

Chihi, L., 1995. Les Fosses Néogène a Quaternaires de la Tunisie de la mer Pelagienne: Leur Signification dans le Cadre Geodynamique de la Méditerranée Centrale. These de Doctorat d'Etat. Université de Tunis II.

Clocchiatti, R., Sassi, S., 1972. Decouverte de temoin d'un volcanisme Paleocene a Eocene dans le bassin phosphate de Metlaoui (Tunisie meridionale). Comptes-Rendus l'Academie des Sci. Paris 513–517.

Coxall, H.K., 2000. Hantkeninid Planktonic Foraminifera and Eocene Palaeoceanographic Change. Thesis. University of Bristol.

Coxall, H.K., Wilson, P.A., Pälike, H., Lear, C.H., Backman, J., 2005. Rapid stepwise onset of Antarctic glaciation and deeper calcite compensation in the Pacific Ocean. Nature 433, 53–57. https://doi.org/10.1038/nature03135.

Curry, D., 1981. Stratotypes of Paleogene Stages. In: Pomerol, C. (Ed.), Bulletin d'information Des Géologues Du Bassin de Paris, Mémoire Hors Série, pp. 23–36.

Dalbiez, F., 1955. The Genus Globotruncana in Tunisia. In: Étude Sommaire Des Microfaunes de La Région Du Kef. Notice Explicative de La Feuille n 44, Le Kef, Carte Géologique de La Tunisie Au 1/50.000, pp. 161–171.

Dawber, C.F., Tripati, A.K., 2011. Constraints on glaciation in the Middle Eocene (46-37 Ma) from Ocean Drilling Program (ODP) Site 1209 in the tropical Pacific Ocean. Paleoceanography 26, 1–17. https://doi.org/10.1029/2010PA002037.

De Vleeschouwer, D., Parnell, A.C., 2014. Reducing time-scale uncertainty for the Devonian by integrating astrochronology and Bayesian statistics. Geology 42, 491–494. https://doi.org/10.1130/G35618.1.

Dunkley Jones, T., Bown, P.R., Pearson, P.N., Wade, B., Coxall, H.k., Lear, C.H., 2008. Major shifts in calcareous phytoplankton assemblages through the Eocene-Oligocene transition of Tanzania and their implications for low-latitude primary production. Paleoceanography 23, 1–14. https://doi.org/10.1029/2008PA001640.

Edgar, K.M., Wilson, P.A., Sexton, P.F., Suganuma, Y., 2007. No extreme bipolar glaciation during the main Eocene calcite compensation shift. Nature 448, 908–911. https://doi.org/10.1038/nature06053.

Edgar, K.M., Wilson, P.A., Sexton, P.F., Gibbs, S.J., Roberts, A.P., Norris, R.D., 2010. New biostratigraphic, magnetostratigraphic and isotopic insights into the Middle Eocene Climatic Optimum in low latitudes. Palaeogeogr. Palaeoclimatol. Palaeoecol. 297, 670–682. https://doi.org/10.1016/j.palaeo.2010.09.016.

Edgar, K.M., Bohaty, S.M., Coxall, H.K., Bown, P.R., Batenburg, S.J., Lear, C.H., Pearson, P.N., 2020. New composite bio- and isotope stratigraphies spanning the Middle Eocene Climatic Optimum at tropical ODP Site 865 in the Pacific Ocean. J. Micropalaeontol. 39, 117–138. https://doi.org/10.5194/jm-39-117-2020.

Eldrett, J.S., Vieira, M., Gallagher, L., Hampton, M., Blaauw, M., Swart, P.K., 2020. Late Cretaceous to Palaeogene carbon isotope, calcareous nannofossil and foraminifera stratigraphy of the Chalk Group, Central North Sea. Mar. Pet. Geol. 104789 https://doi.org/10.1016/j.marpetgeo.2020.104789.

Enay, R., Hantzpergue, P., Soussi, M., Mangold, C., 2005. The Kimmeridgian-Tithonian boundary and age of the upper Jurassic formations of the Tunisian Dorsale, comparisons with Algeria and sicily. Geobios 38, 437–450. https://doi.org/10.1016/j.geobios.2004.01.001.

Exon, N.F., Kennett, J.P., Malone, M.J., 2004. Leg 189 synthesis: Cretaceous-Holocene history of the Tasmanian gateway. Proc. Ocean Drill. Program Sci. Results 189, 1–27. https://doi.org/10.2973/odp.proc.sr.189.101.2004.

Fakhfakh Ben Jemai, H., 2001. Lithostratigraphy, paleontology and reservoir characterisation of the Eocene deposits in Tunisia. In: ETAP, Hydrocarb. Proj. Prog. Report.

Fioroni, C., Villa, G., Persico, D., Jovane, L., 2015. Middle Eocene-lower Oligocene calcareous nannofossil biostratigraphy and paleoceanographic implications from Site 711 (equatorial Indian Ocean). Mar. Micropaleontol. 118, 50–62. https://doi.org/10.1016/j.marmicro.2015.06.001.

Fornaciari, E., Agnini, C., Catanzariti, R., Rio, D., Bolla, E.M., Valvasoni, E., 2010. Mid-latitude calcareous nannofossil biostratigraphy and biochronology across the middle to late eocene transition. Stratigraphy 7, 229–264.

Galeotti, S., DeConto, R.M., Naish, T., Stocchi, P., Florindo, F., Pagani, M., Barrett, P., Bohaty, S.M., Lanci, L., Pollard, D., Sandroni, S., Talarico, F.M., Zachos, J.C., 2016. Antarctic Ice Sheet variability across the Eocene-Oligocene boundary climate transition. Science 80, 353. https://doi.org/10.1126/science.aab0669.

Garzanti, E., Critelli, S., Ingersoll, R.V., 1996. Paleogeographic and paleotectonic evolution of the Himalayan Range as reflected by detrital modes of Tertiary sandstones and modern sands (Indus transect, India and Pakistan). Bull. Geol. Soc. Am. 108, 631–642. https://doi.org/10.1130/0016-7606(1996)108<0631:PAPEOT>2.3.CO;2.

Giorgioni, M., Jovane, L., Rego, E.S., Rodelli, D., Frontalini, F., Coccioni, R., Catanzariti, R., Özcan, E., 2019. Carbon cycle instability and orbital forcing during the Middle Eocene Climatic Optimum. Nature 9, 1–10. https://doi.org/10.1038/s41598-019-45763-2.

Hardenbol, J., Thierry, J., Farley, M.B., Jacquin, T., Graciansky, D., Vail, P.R., 1998. Mesozoic and Cenozoic sequence chronostratigraphic framework of European Basins. In: De Graciansky, P.C., Hardenbol, J., Jacquin, T., Vail, P. (Eds.), Mesozoic and Cenozoic Sequence Stratigraphy of European Basins. SEPM Special Publication, pp. 3–14.

Hay, W.W., Mohler, H.P., Roth, P.H., Schmidt, R.R., Boudreaux, J.E., 1967. Calcareous nannoplankton zonation of the Cenozoic of the Gulf Coast and Carribbean– Antillean area and transoceanic correlation. Trans. Gulf Coast Assoc. Geol. Soc. 17, 428–480.

Henchiri, M., 2007. Sedimentation, depositional environment and diagenesis of Eocene biosiliceous deposits in Gafsa basin (southern Tunisia). J. Afr. Earth Sci. 49, 187–200. https://doi.org/10.1016/j.jafrearsci.2007.09.001.

Henchiri, M., Slim-S'himi, N., 2006. Silicification of sulphate evaporites and their carbonate replacements in Eocene marine sediments, Tunisia: two diagenetic trends. Sedimentology 53, 1135–1159. https://doi.org/10.1111/j.1365-3091.2006.00806.x.

Höntzsch, S., 2011. Palaeogene Carbonate Platforms under Climatic and Tectonic Stress – Case Studies from Egypt and Spain. PhD thesis. University of Bremen.

Hooker, J.J., King, C., 2019. The Bartonian unit stratotype (S. England): Assessment of its correlation problems and potential. Proc. Geol. Assoc. 130, 157–169. https://doi.org/10.1016/j.pgeola.2018.08.005.

Jorry, S., 2004. The Eocene Nummulite Carbonates (Central Tunisia and NE Libya): Sedimentology, Depositional Environments, and Application to Oil Reservoirs. Sci. la Terre Genève. Université de Genève.

Jovane, L., Florindo, F., Coccioni, R., Dinarès-Turell, J., Marsili, A., Monechi, S., Roberts, A.P., Sprovieri, M., 2007a. The middle Eocene climatic optimum event in the Contessa Highway section, Umbrian Apennines, Italy. Bull. Geol. Soc. Am. 119, 413–427. https://doi.org/10.1130/B25917.1.

Jovane, L., Sprovieri, M., Florindo, F., Acton, G., Coccioni, R., Dall'Antonia, B., Dinarès-Turell, J., 2007b. Eocene-Oligocene paleoceanographic changes in the stratotype section, Massignano, Italy: clues from rock magnetism and stable isotopes. J. Geophys. Res. Solid Earth 112, 1–16. https://doi.org/10.1029/2007JB004963.

Jovane, L., Coccioni, R., Marsili, A., Acton, G., 2009. The late Eocene greenhouse-icehouse transition: Observations from the Massignano global stratotype section and point (GSSP). In: Koeberl, C., Montanari, A. (Eds.), The Late Eocene Earth—Hothouse, Icehouse, and Impacts. Geol. Soc. Am, pp. 149–168. https://doi.org/10.1130/2009.2452(10).

Jovane, L., Sprovieri, M., Coccioni, R., Florindo, F., Marsili, A., Laskar, J., 2010. Astronomical calibration of the middle Eocene Contessa Highway section (Gubbio, Italy). Earth Planet. Sci. Lett. 298, 77–88. https://doi.org/10.1016/j.epsl.2010.07.027.

Kennett, J.P., 1977. Cenozoic evolution of Antarctic glaciation, the circum-Antarctic Ocean, and their impact on global paleo-ceanography. J. Geophys. 82, 3843–3860.

Khanolkar, S., Kumar Saraswati, P., Rogers, K., 2017. Ecology of foraminifera during the Middle Eocene climatic optimum in Kutch, India. Geodin. Acta 29, 1–13. https://doi.org/10.1080/09853111.2017.1300846.

Kübler, B., 1987. Cristallinité de l'illite, méthodes normalisées de préparations, méthodes normalisées de mesures. In: Cah. Inst. Géologie Neuchâtel, Suisse, Série ADX.

Kylander, M.E., Klaminder, J., Wohlfarth, B., Löwemark, L., 2013. Geochemical responses to paleoclimatic changes in southern Sweden since the late glacial: the Hässeldala Port lake sediment record. J. Paleolimnol. 50, 57–70. https://doi.org/10.1007/s10933-013-9704-z.

Livermore, R., Nankivell, A., Eagles, G., Morris, P., 2005. Paleogene opening of Drake Passage. Earth Planet. Sci. Lett. 236, 459–470. https://doi.org/10.1016/j.epsl.2005.03.027.

Luciani, V., Giusberti, L., Agnini, C., Fornaciari, E., Rio, D., Spofforth, D.J.A., Pälike, H., 2010. Ecological and evolutionary response of Tethyan planktonic foraminifera to the Middle Eocene Climatic optimum (MECO) from the Alano section (NE Italy). Palaeogeogr. Palaeoclimatol. Palaeoecol. 292, 82–95. https://doi.org/10.1016/j.palaeo.2010.03.029.

Luciani, V., Fornaciari, E., Papazzoni, C.A., Dallanave, E., Giusberti, L., Stefani, C., Amante, E., 2020. Integrated stratigraphy at the Bartonian – Priabonian transition : Correlation between shallow benthic and calcareous plankton zones (Varignano section, northern Italy). Geol. Soc. Am. 1–26.

Marino, M., Flores, J.A., 2002. Middle Eocene to Early Oligocene calcareous nannofossil stratigraphy at Leg 177 Site 1090. Mar. Micropaleontol. 45, 383–398. https://doi.org/10.1016/S0377-8398(02)00036-1.

Martini, E., 1971. Standard palaeogene calcareous nannoplankton zonation. Nature 226, 560–561. https://doi.org/10.1038/226560a0.

Mejri, F., Burollet, F.P., Ben Ferjani, A., Burollet, P.F., Ben Ferjani, A., 2006. Petroleum Geology of Tunisia: A Renewed Synthesis (Entreprise Tunisienne des Activités Pétrolières).

Melki, F., Zouaghi, T., Harrab, S., Sainz, A.C., Bédir, M., Zargouni, F., 2011. Structuring and evolution of Neogene transcurrent basins in the Tellian foreland domain, North-Eastern Tunisia. J. Geodyn. 52, 57–69. https://doi.org/10.1016/j.jog.2010.11.009.

Messaoud, J.H., Thibault, N., Yaich, C., Monkenbusch, J., Omar, H., Ben Jemai, H.F., Watkins, D.K., 2020. The Eocene–Oligocene transition in the South-Western Neo-Tethys (Tunisia): astronomical calibration and paleoenvironmental changes. Paleoceanogr. Paleoclimatol. 35 https://doi.org/10.1029/2020PA003887.

Methner, K., Mulch, A., Fiebig, J., Wacker, U., Gerdes, A., Graham, S.A., Chamberlain, C. P., 2016. Rapid Middle Eocene temperature change in western North America. Earth Planet. Sci. Lett. 450, 132–139. https://doi.org/10.1016/j.epsl.2016.05.053.

Miller, K.G., Fairbanks, R.G., Mountain, G.S., 1987. Tertiary oxygen isotope synthesis, sea level history, and continental margin erosion. Paleoceanography 2, 1–19.

Moiroud, M., Martinez, M., Deconinck, J.F., Monna, F., Pellenard, P., Riquier, L., Company, M., 2012. High-resolution clay mineralogy as a proxy for orbital tuning: example of the Hauterivian-Barremian transition in the Betic Cordillera (SE Spain). Sediment. Geol. 282, 336–346. https://doi.org/10.1016/j.sedgeo.2012.10.004.

Monechi, S., Buccianti, A., Gardin, S., 2000. Biotic signals from nannoflora across the iridium anomaly in the upper Eocene of the Massignano section: evidence from statistical analysis. Mar. Micropaleontol. 39, 219–237. https://doi.org/10.1016/S0377-8398(00)00022-0.

Moon, Y., Zhang, Y.S., Sonn, Y.K., Hyun, B.K., Song, Y., Moon, H.S., 2013. Mineralogical characterization related to physicochemical conditions in the pyrite-rich tailings in Guryong Mine, Korea. Soil Sci. Plant Nutr. 59, 509–521. https://doi.org/10.1080/00380768.2013.773416.

Nieto-Moreno, V., Martínez-Ruiz, F., Giralt, S., Jiménez-Espejo, F., Gallego-Torres, D., Rodrigo-Gámiz, M., García-Orellana, J., Ortega-Huertas, M., De Lange, G.J., 2011. Tracking climate variability in the western Mediterranean during the Late Holocene: a multiproxy approach. Clim. Past 7, 1395–1414. https://doi.org/10.5194/cp-7-1395-2011.

Ogg, J.G., Ogg, G.M., Gradstein, F.M., 2008. The Concise Geologic Time Scale, 177. Cambridge Univ. Press, Cambridge. https://doi.org/10.1016/b978-0-444-59467-9.00001-7.

Ogg, J.G., Ogg, G.M., Gradstein, F.M., 2008. The Concise Geologic Time Scale. Elsevier, Amsterdam, p. 234.

Okada, H., Bukry, D., 1980. Supplementary modification and introduction of code numbers to the low-latitude coccolith biostratigraphic zonation (Bukry, 1973; 1975). Mar. Micropaleontol. 5, 321–325. https://doi.org/10.1016/0377-8398(80)90016-X.

Özcan, E., Less, G., Jovane, L., Catanzariti, R., Frontalini, F., Coccioni, R., Giorgioni, M., Rodelli, D., Rego, E.S., Kayğılı, S., Asgharian Rostami, M., 2019. Integrated biostratigraphy of the middle to upper Eocene Kırkgeçit Formation (Baskil section, Elazığ, eastern Turkey): Larger benthic foraminiferal perspective. In: Mediterranean Geoscience Reviews. Springer International Publishing. https://doi.org/10.1007/s42990-019-00004-6.

Palike, H., Lyle, M., Nishi, H., Raffi, I., Gamage, K., Klaus, A., Scientists, theExpedition 320/321, 2010. Proceedings of the Integrated Ocean Drilling Program (IODP). Integr. Ocean Drillingprogr. Manag. Int. Tokyo, pp. 320–321. https://doi.org/10.2204/iodp.sd.9.01.2010.

Payros, A., Dinares-Turell, J., Monechi, S., Orue-Etxebarria, X., Ortiz, S., Apellaniz, E., Martinez-Braceras, N., 2015. The Lutetian/Bartonian transition (middle Eocene) at the Oyambre section (northern Spain): implications for standard chronostratigraphy. Palaeogeogr. Palaeoclimatol. Palaeoecol. 440, 234–248. https://doi.org/10.1016/j.palaeo.2015.09.015.

Perch-Nielsen, K., 1985. Cenozoic calcareous nannofossils. In: Bolli, H.M., Saunders, J.B., Perch-Nielsen, K. (Eds.), Plankt. Stratigr. Cambridge Univ. Press. Cam- Bridg, pp. 427–554.

Pirlet, H., Wehrmann, L.M., Brunner, B., Frank, N., Dewanckele, J., Van Rooij, D., Foubert, A., Swennen, R., Naudts, L., Boone, M., Cnudde, V., Henriet, J.P., 2010. Diagenetic formation of gypsum and dolomite in a cold-water coral mound in the porcupine seabight, off Ireland. Sedimentology 57, 786–805. https://doi.org/10.1111/j.1365-3091.2009.01119.x.

Ragueneau, O., Savoye, N., Del Amo, Y., Cotten, J., Tardiveau, B., Leynaert, A., 2005. A new method for the measurement of biogenic silica in suspended matter of coastal waters: using Si:Al ratios to correct for the mineral interference. Cont. Shelf Res. 25, 697–710. https://doi.org/10.1016/j.csr.2004.09.017.

Rego, E.S., Jovane, L., Hein, J.R., Sant'Anna, L.G., Giorgioni, M., Rodelli, D., Özcan, E., 2018. Mineralogical evidence for warm and dry climatic conditions in the Neo-Tethys (eastern Turkey) during the middle Eocene. Palaeogeogr. Palaeoclimatol. Palaeoecol. 501, 45–57. https://doi.org/10.1016/j.palaeo.2018.04.007.

Ritsema, C.J., Groenenberg, J.E., 1993. Pyrite oxidation, carbonate weathering, and gypsum formation in a drained potential acid sulfate soil. Soil Sci. Soc. Am. J. 57, 968–976. https://doi.org/10.2136/sssaj1993.03615995005700040015x.

Salamy, K.A., Zachos, J.C., 1999. Latest Eocene – early Oligocene climate change and Southern Ocean fertility : inferences from sediment accumulation and stable isotope data. Palaeogeogr. Palaeoclimatol. Palaeoecol. 145, 61–77.

Savian, J.F., Jovane, L., Frontalini, F., Trindade, R., Coccioni, R., Bohaty, S.M., Wilson, P. A., Florindo, F., Roberts, A.P., Catanzariti, R., Iacoviello, F., 2014. Enhanced primary productivity and magnetotactic bacterial production in response to Middle Eocene warming in the Neo-Tethys Ocean. Palaeogeogr. Palaeoclimatol. Palaeoecol. 414, 32–45. https://doi.org/10.1016/j.palaeo.2014.08.009.

Serra-Kiel, J., Hottinger, L., Caus, E., Drobne, K., Ferrandez, C., KumarJauhri, A., Less, G., Pavlovec, R., Pignatti, J., Samso, J.M., Schaub, H., Sirel, E., Strougo, A., Tambareau, Y., Tosquella, J., Zakrevskaya, E., 1998. Larger foraminiferal biostratigraphy of the Tethyan Paleoceneand Eocene. Bull. Soc. Geol. Fr. 169, 281–299.

Shamrock, J., 2010. Eocene Calcareous nannofossil biostratigraphy , paleoecology and biochronology of ODP Leg 122 Hole 762C , Eastern Indian Ocean (Exmouth Plateau). Stratigraphy 9, 1–54.

Shi, J., Jin, Z., Liu, Q., Zhang, R., Huang, Z., 2019. Cyclostratigraphy and astronomical tuning of the middle eocene terrestrial successions in the Bohai Bay Basin , Eastern China. Glob. Planet. Chang. 174, 115–126. https://doi.org/10.1016/j.gloplacha.2019.01.001.

Sijp, W.P., von der Heydt, A.S., Dijkstra, H.A., Flögel, S., Douglas, P.M.J., Bijl, P.K., 2014. The role of ocean gateways on cooling climate on long time scales. Glob. Planet. Chang. 119, 1–22. https://doi.org/10.1016/j.gloplacha.2014.04.004.

Sluijs, A., Zeebe, R., Bijl, P., Bohaty, S., 2013. A Middle Eocene carbon cycle conundrum. Nat. Geosci. 6, 429–434. https://doi.org/10.1038/ngeo1807.

Soussi, M., Ben Ismaïl, M.H., 2000. Platform collapse and pelagic seamount facies: Jurassic development of Central Tunisia. Sediment. Geol. 133, 93–113. https://doi.org/10.1016/S0037-0738(00)00028-2.

Soussi, M., Enay, R., Boughdiri, M., Mangold, C., Zaghbib-Turki, D., 1999. L'Ammonitico Rosso (formation Zaress) de la dorsale tunisienne. Comptes Rendus l'Academie Sci. - Ser. IIa Sci. la Terre des Planetes 329, 279–286. https://doi.org/10.1016/S1251-8050(99)80247-X.

Spangenberg, J.E., Jacomet, S., Schibler, J., 2006. Chemical analyses of organic residues in archaeological pottery from Arbon Bleiche 3, Switzerland - evidence for dairying in the late Neolithic. J. Archaeol. Sci. 33, 1–13. https://doi.org/10.1016/j.jas.2005.05.013.

Spofforth, D.J.A., Agnini, C., Pälike, H., Rio, D., Fornaciari, E., Giusberti, L., Luciani, V., Lanci, L., Muttoni, G., 2010. Organic carbon burial following the Middle Eocene climatic optimum in the central western Tethys. Paleoceanography 25, 1–11. https://doi.org/10.1029/2009PA001738.

Sprain, C.J., Renne, P.R., Vanderkluysen, L., Pande, K., Self, S., Mittal, T., 2019. The eruptive tempo of deccan volcanism in relation to the cretaceous-paleogene boundary. Science 80 (363), 866–870. https://doi.org/10.1126/science.aav1446.

Thibault, N., Gardin, S., 2006. Maastrichtian calcareous nannofossil biostratigraphy and paleoecology in the Equatorial Atlantic (Demerara Rise , ODP Leg 207 Hole 1258A). Rev. Micropaleontol. 49, 199–214. https://doi.org/10.1016/j.revmic.2006.08.002.

Tlig, S., Sahli, S., Er-Raioui, L., Alouani, R., Mzoughi, M., 2010. Depositional environment controls on petroleum potential of the Eocene in the North of Tunisia. J. Pet. Sci. Eng. 71, 91–105. https://doi.org/10.1016/j.petrol.2010.01.009.

Toffanin, F., Agnini, C., Fornaciari, E., Rio, D., Giusberti, L., Luciani, V., Spofforth, D.J. A., Pälike, H., 2011. Changes in calcareous nannofossil assemblages during the Middle Eocene Climatic Optimum: clues from the central-western Tethys (Alano section, NE Italy). Mar. Micropaleontol. 81, 22–31. https://doi.org/10.1016/j.marmicro.2011.07.002.

Toffanin, F., Agnini, C., Rio, D., Acton, G., Westerhold, T., 2013. Middle Eocene to Early Oligocene calcareous nannofossil biostratigraphy at IODP Site U1333 (equatorial Pacific). Micropaleontology 59, 69–82.

Vahlenkamp, M., Niezgodzki, I., De Vleeschouwer, D., Bickert, T., Harper, D., Kirtland Turner, S., Lohmann, G., Sexton, P., Zachos, J., Pälike, H., 2018. Astronomically paced changes in deep-water circulation in the western North Atlantic during the middle Eocene. Earth Planet. Sci. Lett. 484, 329–340. https://doi.org/10.1016/j.epsl.2017.12.016.

Ver Straeten, C.A., Brett, C.E., Sageman, B.B., 2011. Mudrock sequence stratigraphy: a multi-proxy (sedimentological, paleobiological and geochemical) approach, Devonian Appalachian Basin. Palaeogeogr. Palaeoclimatol. Palaeoecol. 304, 54–73. https://doi.org/10.1016/j.palaeo.2010.10.010.

Villa, G., Fioroni, C., Pea, L., Bohaty, S., Persico, D., 2008. Middle Eocene-late Oligocene climate variability: Calcareous nannofossil response at Kerguelen Plateau, Site 748. Mar. Micropaleontol. 69, 173–192. https://doi.org/10.1016/j.marmicro.2008.07.006.

Wade, B.S., Pearson, P.N., Berggren, W.A., Pälike, H., 2011. Review and revision of Cenozoic tropical planktonic foraminiferal biostratigraphy and calibration to the geomagnetic polarity and astronomical time scale. Earth-Sci. Rev. 104, 111–142. https://doi.org/10.1016/j.earscirev.2010.09.003.

Wei, W., 2004. Opening of the Australia – Antarctica Gateway as dated by nannofossils. Mar. Micropaleontol. 52, 133–152. https://doi.org/10.1016/j.marmicro.2004.04.008.

Westerhold, T., Rohl, U., 2013. Orbital pacing of Eocene climate during the Middle Eocene Climate Optimum and the chron C19r event: missing link found in the tropical western Atlantic. Geochem. Geophys. Geosyst. 14, 4811–4825. https://doi.org/10.1002/ggge.20293.

Westerhold, T., Röhl, U., Pälike, H., Wilkens, R., Wilson, P.A., Acton, G., 2014. Orbitally tuned timescale and astronomical forcing in the middle Eocene to Early Oligocene. Clim. Past 10, 955–973. https://doi.org/10.5194/cp-10-955-2014.

Witkowski, J., Bohaty, S.M., McCartney, K., Harwood, D.M., 2012. Enhanced siliceous plankton productivity in response to middle Eocene warming at Southern Ocean ODP Sites 748 and 749. Palaeogeogr. Palaeoclimatol. Palaeoecol. 326–328, 78–94. https://doi.org/10.1016/j.palaeo.2012.02.006.

Young, J.R., 1990. Size variation of Neogene Reticulofenestra coccoliths from the Indian Ocean DSDP cores. J. Micropalaeontol. 9, 71–85.

Zachos, J.C., 2001. Climate response to orbital forcing across the Oligocene-Miocene boundary. Science 80 (292), 274–278. https://doi.org/10.1126/science.1058288.

Zachos, J.C., Quinn, T.M., Salamy, K.A., 1996. High-resolution 10^4 years deep-sea foraminiferal stable isotope records of the Eocene-Oligocene climate transition. Paleoceanography 11, 251. https://doi.org/10.1029/96PA00571.

Zachos, J.C., Pagani, M., Sloan, L., Thomas, E., Billups, K., 2001. Trends , rhythms , and aberrations in global climate 65 Ma to present. Science 80 (292), 686–694.

Zachos, J.C., Dickens, G.R., Zeebe, R.E., 2008. An early Cenozoic perspective on greenhouse warming and carbon-cycle dynamics. Nature 451, 279–283. https://doi.org/10.1038/nature06588.

Zaïer, A., Beji-Sassi, A., Sassi, S., Moody, R.T.J., 1998. Basin evolution and deposition during the Early Paleogene in Tunisia. Geol. Soc. Spec. Publ. 132, 375–393. https://doi.org/10.1144/GSL.SP.1998.132.01.21.